JACS
JOURNAL OF THE AMERICAN CHEMICAL SOCIETY
pubs.acs.org/JACS
Article

Metal–Ligand Cooperativity via Exchange Coupling Promotes Iron-Catalyzed Electrochemical CO_2 Reduction at Low Overpotentials

Jeffrey S. Derrick, Matthias Loipersberger, Ruchira Chatterjee, Diana A. Iovan, Peter T. Smith, Khetpakorn Chakarawet, Junko Yano, Jeffrey R. Long, Martin Head-Gordon, and Christopher J. Chang*

Cite This: J. Am. Chem. Soc. 2020, 142, 20489–20501

ABSTRACT: Biological and heterogeneous catalysts for the electrochemical CO_2 reduction reaction (CO_2RR) often exhibit a high degree of electronic delocalization that serves to minimize overpotential and maximize selectivity over the hydrogen evolution reaction (HER). Here, we report a molecular iron(II) system that captures this design concept in a homogeneous setting through the use of a redox non-innocent terpyridine-based pentapyridine ligand (tpyPY2Me). As a result of strong metal–ligand exchange coupling between the Fe(II) center and ligand, $[Fe(tpyPY2Me)]^{2+}$ exhibits redox behavior at potentials 640 mV more positive than the isostructural $[Zn(tpyPY2Me)]^{2+}$ analog containing the redox-inactive Zn(II) ion. This shift in redox potential is attributed to the requirement for both an open-shell metal ion and a redox non-innocent ligand. The metal–ligand cooperativity in $[Fe(tpyPY2Me)]^{2+}$ drives the electrochemical reduction of CO_2 to CO at low overpotentials with high selectivity for CO_2RR (>90%) and turnover frequencies of 100 000 s^{-1} with no degradation over 20 h. The decrease in the thermodynamic barrier engendered by this coupling also enables homogeneous CO_2 reduction catalysis in water without compromising selectivity or rates. Synthesis of the two-electron reduction product, $[Fe(tpyPY2Me)]^0$, and characterization by X-ray crystallography, Mössbauer spectroscopy, X-ray absorption spectroscopy (XAS), variable temperature NMR, and density functional theory (DFT) calculations, support assignment of an open-shell singlet electronic structure that maintains a formal Fe(II) oxidation state with a doubly reduced ligand system. This work provides a starting point for the design of systems that exploit metal–ligand cooperativity for electrocatalysis where the electrochemical potential of redox non-innocent ligands can be tuned through secondary metal-dependent interactions.

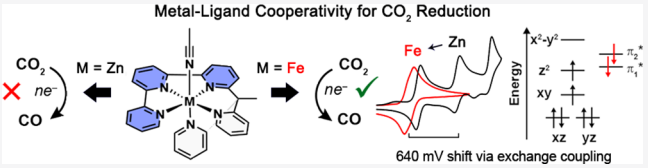

INTRODUCTION

The electrochemical carbon dioxide reduction reaction (CO_2RR) provides opportunities to synthesize value-added products from this greenhouse gas in a sustainable manner.[1,2] Efficient catalysts for this reaction are required to selectively drive CO_2 reduction over the thermodynamic and kinetically competitive hydrogen evolution reaction (HER).[3] Biological,[4] heterogeneous,[5] and molecular[3] catalysts have been studied for CO_2 reduction, and molecular systems in particular offer potential advantages such as their small size relative to enzymes and the fact that they can be tuned with a level of atomic precision that is inaccessible with heterogeneous materials.[6] However, despite advances in the development of molecular catalysts with highly specialized ligand scaffolds, including cyclams,[7−10] porphyrins and phthalocyanines,[11−15] and tricarbonyl-bipyridines,[16,17] it remains a challenge to design molecules that exhibit low overpotentials, high turnover numbers, and compatibility with aqueous electrolytes to avoid off-pathway HER processes. In this regard, one key advantage of biological and heterogeneous catalysts is their ability to minimize overpotential and maximize selectivity for CO_2 reduction via electronic delocalization, either through electron-tunneling pathways[18,19] or a high local density of states,[20−22] respectively. Such systems can thereby achieve organization and separation of reducing equivalents in a way that is challenging to design in molecular systems.

Previous work from our laboratories has explored the chemistry of the $PY5Me_2$ ligand (2,6-bis(1,1-bis(2-pyridyl)-ethyl)pyridine) and its molybdenum[23−25] and cobalt[25,26] derivatives as catalysts for the HER. We reasoned that by incorporating a redox-active pendant such as terpyridine[27−29] within this ligand scaffold, it would be possible to increase metal–ligand orbital mixing and delocalization of electron density away from the metal center to favor CO_2 reduction (Figure 1). Precedent for the use of redox non-innocent ligands in molecular electrochemical CO_2RR has shown the viability of this strategy,[16,17,27−39] along with classic systems bearing strong metal–ligand cooperativity such as metal-dithiolenes for HER.[40−43] Indeed, the suppression of metal-centered reduc-

Received: October 7, 2020
Published: November 18, 2020

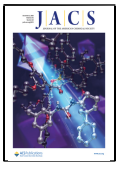

https://dx.doi.org/10.1021/jacs.0c10664
J. Am. Chem. Soc. 2020, 142, 20489−20501

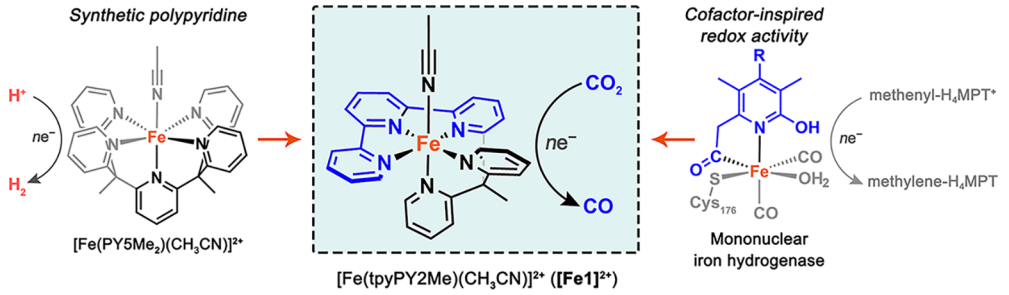

Figure 1. Bioinspired design of a molecular iron polypyridyl complex for electrochemical carbon dioxide reduction catalysis. The molecular CO_2 reduction catalyst $[\mathbf{Fe1}]^{2+}$ was designed to feature a mononuclear iron center supported by a redox-active pendant in a robust synthetic polypyridyl scaffold, inspired by the active site of mononuclear iron hydrogenase.

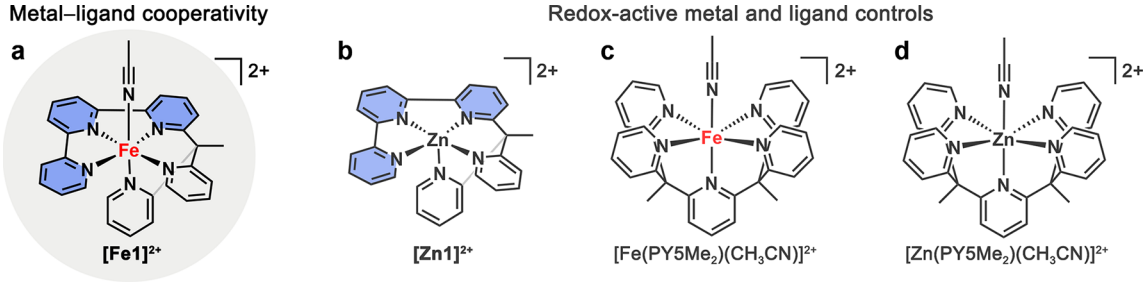

Figure 2. Chemical structures of $[\mathbf{Fe1}]^{2+}$ and the coordination complexes used as controls to disentangle the contributions of the ligand and the metal center in catalysis. (a) Chemical structure of $[\mathbf{Fe1}]^{2+}$ highlighting cooperativity between the open-shell iron center and redox non-innocent tpyPY2Me ligand. (b) The diamagnetic analog containing the redox-silent Zn(II) center, $[\mathbf{Zn1}]^{2+}$, enables the role of the iron center to be probed with the same redox non-innocent ligand scaffold. Likewise, (c) $[Fe(PY5Me_2)(CH_3CN)]^{2+}$ and (d) $[Zn(PY5Me_2)(CH_3CN)]^{2+}$ both feature the redox-innocent $PY5Me_2$ as a related pentapyridine ligand and thus aid in identifying the contributions of the redox-active terpyridine fragment within the polypyridyl scaffold.

tions can limit the formation of off-pathway metal hydride intermediates necessary for hydrogen evolution[35,44] and thereby favor CO_2 reduction catalysis. As part of a larger program in electrocatalysis via bioinorganic mimicry,[6,24,25,45−48] our synthetic approach was inspired by mononuclear iron hydrogenase enzymes, which catalyze the reduction of methenyl-H_4MPT^+ to methylene-H_4MPT in methanogenic archaea.[49] In these systems, heterolysis of H_2 and hydride shuttling is enabled by a single redox-innocent iron(II) site that synergistically interacts with a redox non-innocent guanyl pyridinol cofactor in the primary coordination sphere to provide reducing equivalents (Figure 1).

Here we report an iron polypyridine complex $[Fe(tpyPY2Me)(CH_3CN)]^{2+}$ ($[\mathbf{Fe1}]^{2+}$) (tpyPY2Me = 6-(1,1-di(pyridin-2-yl)ethyl)-2,2′:6′,2″-terpyridine), which features a redox-active terpyridine fragment and demonstrates this principle of electronic delocalization. In particular, metal−ligand cooperativity promotes strong exchange coupling between the redox-active tpyPY2Me ligand and iron(II) center where the $[Fe(tpyPY2Me)]^{2+}$ complex is able to accept two electrons at reduction potentials that are 640 mV more positive than the isostructural $[Zn(tpyPY2Me)]^{2+}$ analog containing the redox-inactive Zn(II) ion, showing that a redox non-innocent ligand alone is not sufficient to promote multielectron redox chemistry with low activation barriers. Upon two-electron reduction of $[Fe(tpyPY2Me)]^{2+}$, strong antiferromagnetic coupling facilitates electrocatalytic reduction of CO_2 to CO at low overpotentials. Under these conditions, $[\mathbf{Fe1}]^{2+}$ exhibits high selectivity for CO production (greater than 90%) at high turnover frequencies. Synthetic reduction of the $[Fe(tpyPY2Me)]^{2+}$ complex enables access to the hypothesized catalytically active species, $[Fe(tpyPY2Me)]^0$, which has been characterized by X-ray crystallography, Mössbauer spectroscopy, X-ray absorption spectroscopy (XAS), variable temperature NMR, and density functional theory (DFT) calculations. The collective data support assignment of an open-shell singlet ground state that maintains a formal Fe(II) oxidation state, comprised of an intermediate-spin iron(II) ($S_{Fe} = 1$) antiferromagnetically coupled to a doubly reduced triplet terpyridine ligand ($S_{tpy} = 1$). This electronic structure also enables the molecular catalyst to operate at low overpotentials in both organic and neutral aqueous electrolytes, resulting in high selectivity for CO_2RR over HER.

RESULTS AND DISCUSSION

Design, Synthesis, and Characterization of the Redox Non-Innocent tpyPY2Me Ligand and Its Metal Coordination Complexes Showing Deviations from Idealized Octahedral Geometry. The tpyPY2Me ligand and corresponding iron(II) complex $[Fe(tpyPY2Me)]^{2+}$, abbreviated as $[\mathbf{Fe1}]^{2+}$, were prepared following modifications of previously reported procedures for the pentapyridine $PY5Me_2$ ligand and its metal complexes (see Supporting Information). Briefly, the pentapyridine ligand tpyPY2Me bearing a redox non-innocent terpyridine fragment was formed by a lithium-mediated coupling between 6-bromo-2,2′:6′,2″-terpyridine and 2,2′-(ethane-1,1-diyl)dipyridine. A series of control coordination complexes were synthesized and evaluated to disentangle the contributions of the redox-active ligand from the metal center (Figure 2). In order to decipher the role of the iron center in electrochemical behavior and subsequent catalysis, we prepared the diamagnetic, isostructural zinc(II) analog $[Zn(tpyPY2Me)]^{2+}$ ($[\mathbf{Zn1}]^{2+}$) that is equipped with the same redox-active tpyPY2Me ligand but with a redox-silent zinc

https://dx.doi.org/10.1021/jacs.0c10664
J. Am. Chem. Soc. 2020, 142, 20489−20501

center. To aid in identifying the role of the redox-active terpyridine fragment of the polypyridyl scaffold, $[Fe(PY5Me_2)(CH_3CN)]^{2+}$ [50] and $[Zn(PY5Me_2)(CH_3CN)]^{2+}$ [26] complexes bearing the related pentapyridine $PY5Me_2$ ligand without polypyridine conjugation were synthesized. Indeed, irreversible reduction of the $PY5Me_2$ ligand occurs at very negative potentials (between −2.0 and −2.5 V vs Fc/Fc^+) and is coupled to catalyst decomposition; thus it serves as a polypyridyl redox-innocent ligand control (Figure 2).

A comparison of the solid-state structures of $[\mathbf{Fe1}]^{2+}$ and $[Fe(PY5Me_2)(CH_3CN)]^{2+}$[50] obtained via single-crystal X-ray diffraction (XRD) revealed that the enhanced rigidity of the tpyPY2Me ligand enforces a more distorted *pseudo*-octahedral (O_h) geometry in $[\mathbf{Fe1}]^{2+}$ relative to $[Fe(PY5Me_2)(CH_3CN)]^{2+}$, which adopts an almost ideal O_h geometry (Figure 3a; Tables S1 and S2). In particular, occupation of the iron equatorial plane by the three terpyridine nitrogen atoms and coordination of the pyridine arms to axial and equatorial positions induces severe axial distortions in $[\mathbf{Fe1}]^{2+}$ that are absent in $[Fe(PY5Me_2)(CH_3CN)]^{2+}$ (Table S2). This distortion also significantly compresses the axial bond angle in $[\mathbf{Fe1}]^{2+}$ (173.64(6)°) whereas the corresponding angle in $[Fe(PY5Me_2)(CH_3CN)]^{2+}$ is nearly linear (178.53(7)°) (Figure 3a). Distortion of the primary coordination sphere as a result of the enhanced ligand rigidity of tpyPY2Me is also observed for the control analog bearing the redox-silent Zn(II) center, $[\mathbf{Zn1}]^{2+}$. The solid-state structure of $[\mathbf{Zn1}]^{2+}$ (Figure S1; Tables S3 and S4) shows that tpyPY2Me enforces a severely distorted square pyramidal coordination geometry with the terpyridine nitrogen atoms occupying equatorial positions. This structure departs quite significantly from the O_h geometry observed for $[Zn(PY5Me_2)(CH_3CN)]^{2+}$.[26]

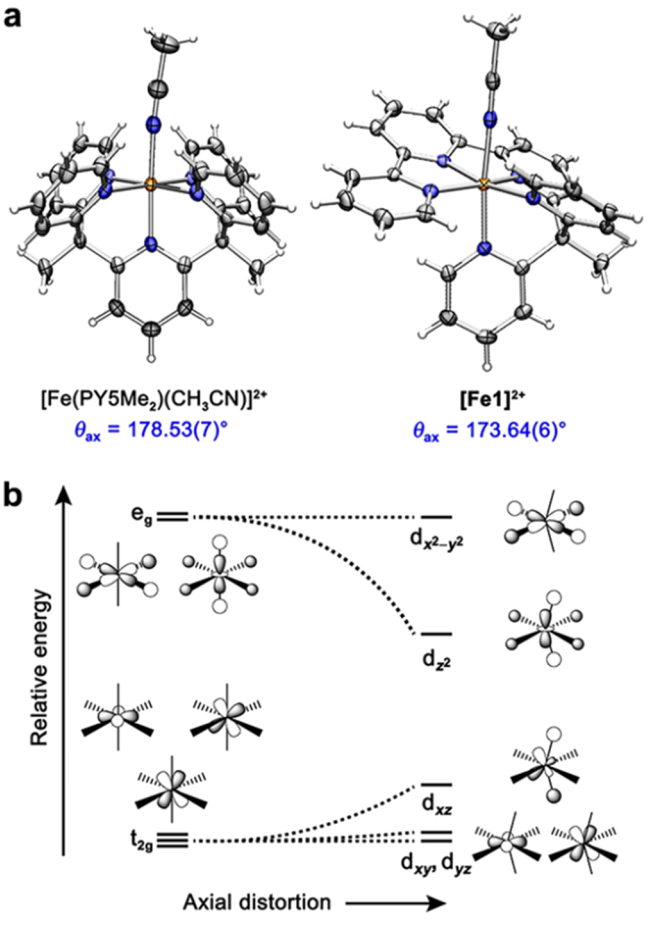

Figure 3. Structural characterization of iron polypyridyl complexes. (a) Solid state structures of $[Fe(PY5Me_2)(CH_3CN)]^{2+}$, featuring the redox-innocent $PY5Me_2$ ligand, and $[\mathbf{Fe1}]^{2+}$, as determined via X-ray diffraction analysis. Thermal ellipsoids are plotted at 80% probability level; orange, blue, and gray ellipsoids represent Fe, N, and C atoms, respectively. Non-coordinating solvent and anions are omitted for clarity. (b) Simplified Walsh diagram illustrating the effect of axial distortion away from the near ideal O_h symmetry in $[Fe(PY5Me_2)(CH_3CN)]^{2+}$ toward C_{2v} symmetry in $[\mathbf{Fe1}]^{2+}$.

The structure of $[\mathbf{Fe1}]^{2+}$ remains more distorted than that of $[Fe(PY5Me_2)(CH_3CN)]^{2+}$ in solution, as verified by ^{1}H NMR spectra collected for both complexes in CD_3CN at 295 K. The ^{1}H NMR spectrum of $Fe(PY5Me_2)(CH_3CN)]^{2+}$ features five sharp signals consistent with a C_{2v} symmetric complex with low-spin Fe(II) ($S = 0$), whereas the ^{1}H NMR spectrum of $[\mathbf{Fe1}]^{2+}$ features slightly more broadened resonances with no well-defined symmetry (Figure S2). Alternatively, $[\mathbf{Zn1}]^{2+}$ shows a ^{1}H NMR spectrum with all expected ligand resonances accounted for, consistent with its diamagnetic ground state (see Supporting Information). Using the Evans method, we measured an effective magnetic moment (μ_{eff}) of 1.27 μ_B for $[\mathbf{Fe1}]^{2+}$ at 293 K, which is indicative of a low-spin Fe(II) ground state ($S = 0$) with a population of thermally accessible spin excited states at room temperature (Figure S3). Because the $[\mathbf{Fe1}]^{2+}$ bond lengths measured at 100 K are in agreement with those of other low-spin Fe(II) polypyridyl complexes,[50] the collective data suggest that $[\mathbf{Fe1}]^{2+}$ undergoes a spin-state transition between 100 K and room temperature. To further probe the spin-state transition of $[\mathbf{Fe1}]^{2+}$, variable-temperature (VT) ^{1}H NMR spectra were collected in CD_3CN across a temperature range of 233 to 353 K (Figure S4). At 293 K, resonances at 9.47, 7.73, 7.12, and 6.74 ppm appear as very broad singlets and upon heating the sample to 353 K, these peaks become undetectable due to broadening into the baseline (Figure S4b). Upon stepwise cooling, the resonances start to become fully resolved. At 233 K, integration of the aryl region accounts for the 18 proton signals expected for $[\mathbf{Fe1}]^{2+}$. This temperature-dependent signal broadening is in line with our interpretation of a population of thermally accessible spin excited states. Due to the absence of systematic, temperature-dependent paramagnetic shifts of the $[\mathbf{Fe1}]^{2+}$ resonances, we were unable to quantify the spin equilibrium from the ^{1}H NMR data alone. Nevertheless, variable temperature Evans method data further revealed a gradual increase in μ_{eff} upon heating, in agreement with the occurrence of a spin transition process in solution (Figure S5). The limited temperature range available in acetonitrile and limited solubility of $[\mathbf{Fe1}]^{2+}$ in alternative solvents to expand this temperature range prevents isolation of a pure population of low-spin Fe(II) (μ_{eff} of 1.20 μ_B at 233 K) and the transition is incomplete at the highest available temperature (μ_{eff} of 1.33 μ_B at 353 K), precluding accurate determination of the spin-equilibrium transition ($T_{1/2}$).

Zero-field ^{57}Fe Mössbauer spectra collected for $[\mathbf{Fe1}]^{2+}$ at 5 and 295 K further support such a spin state transition for the Fe(II) center (Figure S6 and Tables S5). At 5 K, the spectrum features a symmetric Lorentzian doublet with isomer shift (δ) and quadrupole splitting ($|\Delta E_Q|$) values of 0.3562(4) and 1.0203(8) mm/s, respectively, consistent with a low-spin iron(II) (Figure S6a and Tables S5). The density functional theory (DFT) computed Mössbauer parameters closely match the experimental values within the well-established uncertainty

https://dx.doi.org/10.1021/jacs.0c10664
J. Am. Chem. Soc. 2020, 142, 20489−20501

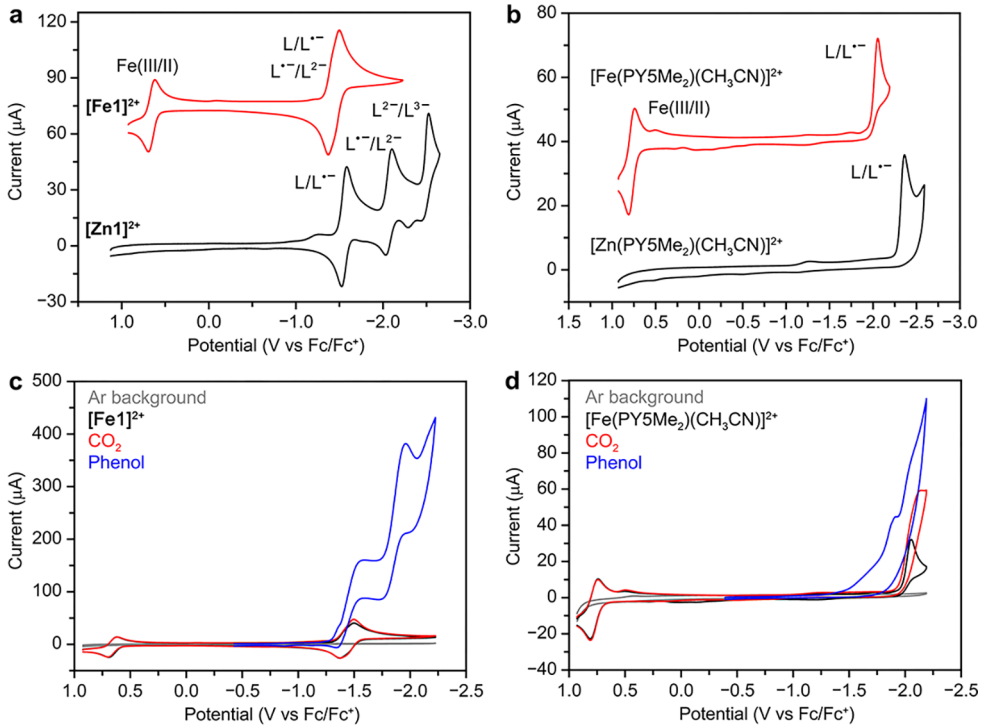

Figure 4. Electrochemical characterization. Cyclic voltammograms collected under Ar of (a) $[\mathbf{Fe1}]^{2+}$ (red trace) and $[\mathbf{Zn1}]^{2+}$ (black trace) complexes and (b) $[Fe(PY5Me_2)(CH_3CN)]^{2+}$ (red trace) and $[Zn(PY5Me_2)(CH_3CN)]^{2+}$ (black trace) complexes supported by redox-innocent $PY5Me_2$. These data show that the unique combination of Fe and redox non-innocent tpyPY2Me ligand lead to electrochemically reversible two-electron chemistry, with the Zn-tpyPY2Me analog exhibiting two reversible one-electron reduction waves with the second reduction at potentials 640 mV more negative than the iron analog. The Fe(II) and Zn(II) $PY5Me_2$ analogs both exhibit irreversible electrochemical reductions at potentials more negative than −2.0 V vs Fc/Fc^+. Cyclic voltammograms of (c) $[\mathbf{Fe1}]^{2+}$ and (d) $[Fe(PY5Me_2)(CH_3CN)]^{2+}$ collected under Ar (black), CO_2 (red), and with added phenol (3.5 M, blue). Voltammograms were collected with a scan rate of 100 mV/s with an electrolyte of 0.10 M $TBAPF_6$ dissolved in CH_3CN.

ranges (~0.10 mm/s for δ and ~0.3 mm/s for $|\Delta E_Q|$),[51,52] thus corroborating the low-spin Fe(II) assignment (Figure S7 and Table S6). In contrast, the Mössbauer spectrum measured at 295 K features an asymmetric quadrupole doublet that can be fit to two different iron sites (Figure S6b and Table S5). The parameters of the major site are nearly identical to the 5 K spectrum when accounting for second-order Doppler shifts (SODS) (δ = 0.285(1) mm/s, $|\Delta E_Q|$ = 1.056(2) mm/s) and are therefore consistent with the same low-spin Fe(II) species observed at 5 K. The isomer shift of the minor site is significantly more positive (0.62(1) mm/s) and is indicative of a higher spin iron(II) species. DFT predicted Mössbauer parameters for these higher-spin Fe(II) species correspond closely to the experimental values for the minor site measured at 295 K, further supporting this assignment (Figure S7 and Table S6).

The distinct iron(II) spin states in $[\mathbf{Fe1}]^{2+}$ and $[Fe(PY5Me_2)(CH_3CN)]^{2+}$ can be understood from the simplified Walsh diagram presented in Figure 3b. Axial distortions engendered by the rigid tpyPY2Me ligand lead to a decrease in symmetry from idealized O_h to C_{2v}, and this distortion significantly stabilizes the d_{z^2} orbital and destabilizes the d_{xz} through z-component mixing of the t_{1u} and t_{2g} orbitals. The stabilization of the d_{z^2} orbital and disruption of t_{2g} degeneracy can then facilitate the formation of thermally accessible spin excited states near room temperature. We hypothesize that these marked differences in the ground-state electronic structures of $[\mathbf{Fe1}]^{2+}$ and $Fe(PY5Me_2)(CH_3CN)]^{2+}$ contribute to their distinct electrochemical and catalytic behavior (*vide infra*).

Cyclic Voltammetry of tpyPY2Me Fe(II) and Zn(II) Complexes and Comparison to $PY5Me_2$ Analogs Lacking the Redox Non-Innocent Terpyridine Fragment.

The presence of a redox-active terpyridine moiety in tpyPY2Me also gives rise to unique electrochemical behavior for $[\mathbf{Fe1}]^{2+}$ and $[\mathbf{Zn1}]^{2+}$ relative to their $PY5Me_2$ analogues. The room-temperature cyclic voltammogram (CV) of $[\mathbf{Fe1}]^{2+}$ collected in CH_3CN under Ar exhibits three reversible features: a one-electron oxidation at $E_{1/2}$ = 0.66 V (versus Fc/Fc^+) assigned to the iron(III/II) couple and two, closely spaced, one-electron redox processes that are centered at −1.43 V (Figure 4a). Further chemical characterization of this redox behavior indicates that these redox events are two sequential ligand-based reductions ($tpyPY2Me^{0/1-}$ and $tpyPY2Me^{1-/2-}$) (*vide infra*). During constant potential coulometry of 7.6×10^{-3} mmol of $[\mathbf{Fe1}]^{2+}$ conducted at −1.60 V vs Fc/Fc^+ under Ar atmosphere, 1.58 C of charge was passed equating to 2.1 electrons per molecule of $[\mathbf{Fe1}]^{2+}$, supporting this assignment as two closely spaced one-electron redox waves centered at −1.43 V vs Fc/Fc^+ (Figure S8). No additional features were observed when scanning to more negative potentials.

In contrast, under the same conditions, the cyclic voltammogram of $[\mathbf{Zn1}]^{2+}$ exhibits two, well-separated, reversible, one-electron ligand-centered reductions with $E_{1/2}$ of −1.56 and −2.07 V as well as an additional irreversible redox event (tentatively assigned as $tpyPY2Me^{2-/3-}$) at −2.41 V (Figure 4a). The first ligand centered reduction of $[\mathbf{Zn1}]^{2+}$ occurs at a comparable potential to that of $[\mathbf{Fe1}]^{2+}$ but the second ligand centered reduction is shifted 640 mV more negative and it is this disparate electrochemical behavior between $[\mathbf{Fe1}]^{2+}$ and $[\mathbf{Zn1}]^{2+}$ that indicates a degree of communication between the reduced tpyPY2Me ligand and the open-shell iron center

https://dx.doi.org/10.1021/jacs.0c10664
J. Am. Chem. Soc. 2020, 142, 20489−20501

that is not possible in the isostructural complex containing the closed-shell, redox-silent zinc center. In contrast, ligand-based reductions in $[Fe(PY5Me_2)(CH_3CN)]^{2+}$ and $[Zn(PY5Me_2)(CH_3CN)]^{2+}$ are electrochemically irreversible and occur at potentials negative of −2.0 V (Figure 4b), highlighting the crucial role of the terpyridyl fragment in achieving electrochemically reversible reduction events at relatively positive potentials.

Electrochemical Reduction of CO_2 Catalyzed by $[Fe(tpyPY2Me)]^{2+}$ in Organic Solution. Under an atmosphere of CO_2, CV data collected for $[\mathbf{Fe1}]^{2+}$ exhibit only a subtle increase in current relative to scans under Ar; however, when excess phenol (3.5 M) is added as a proton source, two large catalytic waves appear at ca. −1.50 and −2.0 V versus Fc/Fc^+ (Figure 4c). The $PY5Me_2$ analog $[Fe(PY5Me_2)(CH_3CN)]^{2+}$ also displays catalytic currents upon addition of CO_2 and phenol, but the onset current for catalysis is >500 mV more negative than that observed for $[\mathbf{Fe1}]^{2+}$ (Figure 4d). Phenol titrations conducted with solutions of $[\mathbf{Fe1}]^{2+}$ under a CO_2 atmosphere revealed a dose-dependence on phenol concentration (Figure S9a). The electrochemical response is mitigated when control phenol titrations are collected under an Ar atmosphere, suggesting that $[\mathbf{Fe1}]^{2+}$ selectively catalyzes electrochemical CO_2 reduction (CO_2RR) over the hydrogen evolution reaction (HER), even at high concentrations of organic acid (Figure S9b). As anticipated, the isostructural Zn(II) analog $[\mathbf{Zn1}]^{2+}$ does not show similar increases in catalytic current at such positive potentials (Figure S10), establishing that the redox non-innocent tpyPY2Me ligand alone with a Lewis acid center is not sufficient for promoting CO_2RR activity.

Controlled Potential Electrolysis Studies for Direct Product Measurements of Electrochemical CO_2RR Catalyzed by $[Fe(tpyPY2Me)]^{2+}$ in Organic Solution. Preparative-scale controlled potential electrolysis (CPE) experiments were conducted in CO_2-saturated acetonitrile with 3.5 M phenol across a range of applied potentials (−1.35 to −1.98 V vs Fc/Fc^+), and the products were quantified by gas chromatography. We find that CO is the major product of CO_2RR. Importantly, we note that subsequent turnover number and turnover rate values reported in this work are derived from these direct measurements of product, as opposed to indirect methods derived from transient CV currents with electrochemical assumptions.

Because the utility of a catalyst is benchmarked by its rate and overpotential (η), the applied potentials were also converted into overpotentials following the methods reported by Mayer[53] and Matsubara and co-workers.[54,55] Accurate conversion necessitates that the thermodynamic potential for CO_2 reduction to CO is known under the experimental conditions. Whereas the aqueous standard potential is known (−0.106 V vs SHE;[56] −0.730 V vs Fc/Fc^+ [57]), it is difficult to experimentally determine in organic solvents where the identity and amount of the proton source complicate the measurements. This caveat often leads to the use of estimated values that do not match the experimental conditions or rely on thermodynamic assumptions that do not rigorously apply, such as taking the CO_2 and CO standard states to be 1 M[13,14] or assuming anhydrous conditions without reporting measured water concentrations or using anhydrous organic acids,[58] leading to potential inconsistencies in the literature with regard to reported overpotentials. With the goal of increasing standardization and transparency in molecular electrocatalysis, we report the applied potentials from our CPE experiments in both overpotential and versus Fc/Fc^+ and use a conservative estimate of $E^0_{CO_2/CO}$ (−1.27 V vs Fc/Fc^+)[55] obtained from measured pK_a values for acetonitrile−water mixtures (see Supporting Information for additional details). It should be noted that this value is 770 mV more positive than for "dry" acetonitrile and 70 mV more positive than the previously estimated standard redox potential for "wet" acetonitrile derived by assigning unusual gas standard states.[13,14] Tafel plots that compare catalyst activity are plotted to show both the calculated overpotential as well as the directly measured potential versus the reference electrode used in the experiments. We reason that reporting both values should lead to more clarity in benchmarking catalysts.

$[\mathbf{Fe1}]^{2+}$ is highly selective for CO_2 reduction over hydrogen evolution across the entire potential window examined (Figure 5a and Figures S11 and S12; Table S7), with averaged specific current densities for CO production (j_{CO}) reaching as high as 3.6 mA/cm^2 (Figure 5a and Figures S11 and S12; Table S7). The

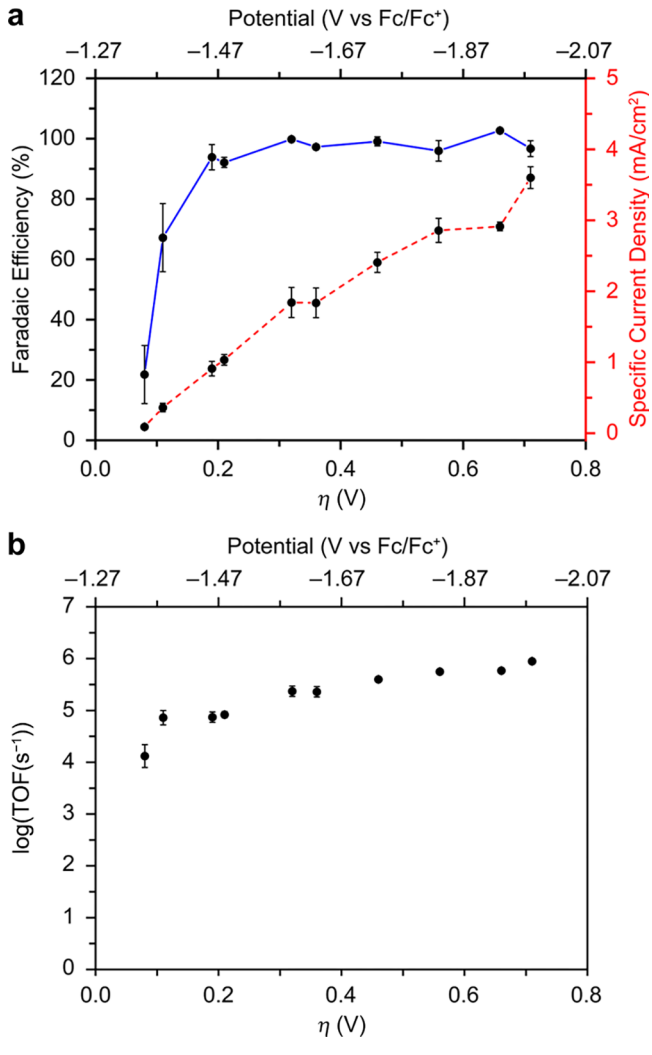

Figure 5. Electrochemical CO_2 reduction performance of $[\mathbf{Fe1}]^{2+}$. (a) Selectivity of $[\mathbf{Fe1}]^{2+}$ for CO_2 reduction to CO at varying overpotentials and specific current densities for CO (j_{CO}) production (averages of three experiments). (b) Catalytic Tafel plot for $[\mathbf{Fe1}]^{2+}$ obtained from CPE experiments in acetonitrile with added phenol (3.5 M). CPE experiments were collected in an electrolyte of 0.10 M $TBAPF_6$ dissolved in CH_3CN.

https://dx.doi.org/10.1021/jacs.0c10664
J. Am. Chem. Soc. 2020, 142, 20489−20501

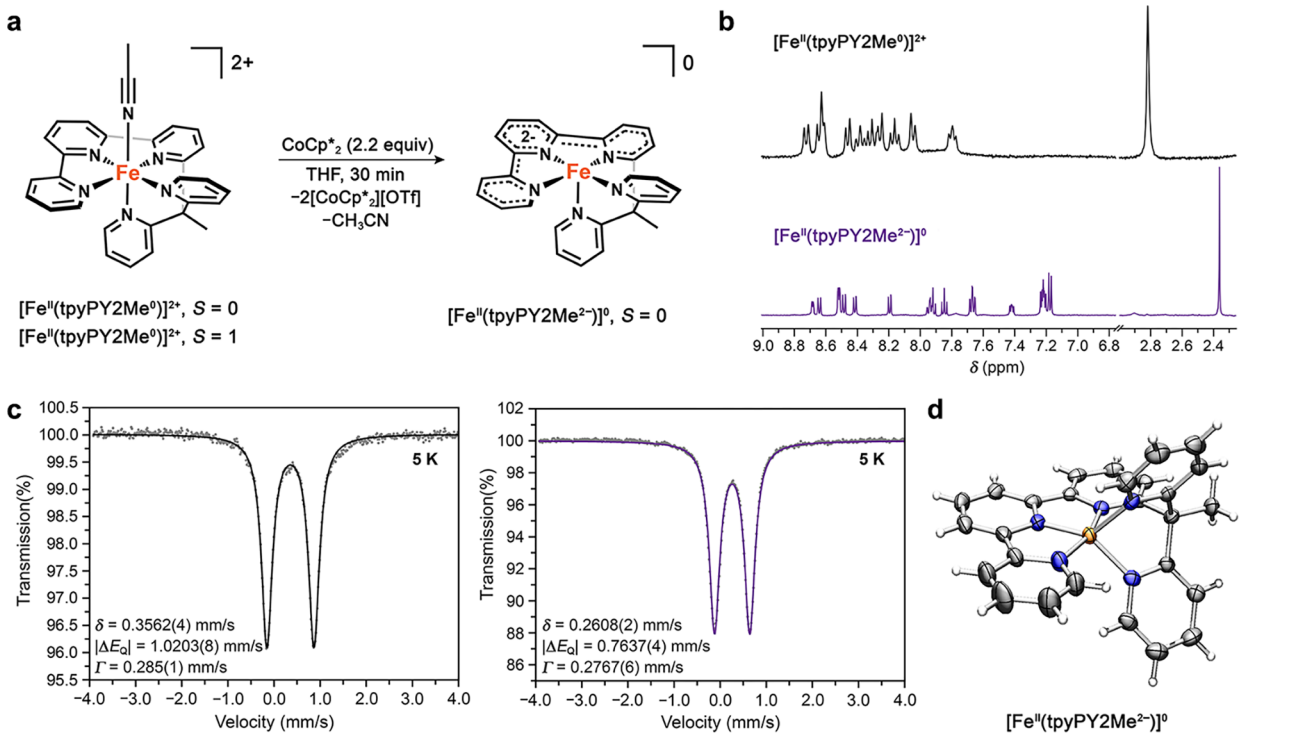

Figure 6. Synthetic preparation and characterization of the two-electron reduced species $[\mathbf{Fe1}]^0$. The collective structural and spectroscopic data support assignment to an open-shell singlet species that maintains a formal Fe(II) oxidation state. (a) Two-electron reduction of $[\mathbf{Fe1}]^{2+}$ generates the $[\mathbf{Fe1}]^0$ complex that is a putatively active species for CO_2 reduction. (b) ^{1}H NMR spectrum of $[\mathbf{Fe1}]^{2+}$ (black) and ^{1}H NMR spectrum of the product resulting from chemical reduction of $[\mathbf{Fe1}]^{2+}$ with $CoCp^*_2$ (purple); both spectra were in CD_3CN at room temperature. (c) Zero-field ^{57}Fe Mössbauer analysis of $[\mathbf{Fe1}]^{2+}$ (black) and $[\mathbf{Fe1}]^0$ (purple) measured at 5 K. (d) Solid-state structure of $[\mathbf{Fe1}]^0$ from single-crystal X-ray diffraction analysis. Thermal ellipsoids are plotted at 80% probability level; orange, blue, and gray ellipsoids represent Fe, N, and C atoms, respectively. Residual solvent and co-crystallized $CoCp^*_2$ are omitted for clarity.

Faradaic efficiency for CO production (FE_{CO}) reaches 94% at an overpotential of 190 mV (−1.46 V vs Fc/Fc^+) and increases to 100% with the application of overpotentials between 320 and 710 mV (−1.59 and −1.98 V vs Fc/Fc^+) (Figure 5a and Figure S11; Table S7). This high activity and selectivity for CO production at applied potentials as low as −1.46 V vs Fc/Fc^+ is a substantial decrease in the energy requirements compared to other molecular catalysts and sits among the most efficient reported catalysts.[14,27−29,59−61] Significantly, no CO and only small amounts of H_2 (FE_{H_2} = 44%) were detected in analogous CPE experiments with $[Fe(PY5Me_2)(CH_3CN)]^{2+}$ at much larger overpotentials (Figure S13). Moreover, variable potential CPE experiments with $[\mathbf{Zn1}]^{2+}$ conducted between −1.66 V and −2.41 V vs Fc/Fc^+ produced only trace amounts of CO (FE_{CO} = 1−6%) and a small amount of H_2 (FE_{H_2} = 1−20%), further illustrating the importance of metal−ligand cooperativity for efficient CO_2RR catalysis (Figure S14).

Control experiments strongly support the homogeneous molecular nature of $[\mathbf{Fe1}]^{2+}$. First, CO_2 reduction was not observed in the absence of $[\mathbf{Fe1}]^{2+}$ (Figure S15). Furthermore, cyclic voltammetry and UV−vis data collected before and after 1 h CPE experiments are indistinguishable, attesting to the bulk stability of $[\mathbf{Fe1}]^{2+}$ under electrolysis conditions (Figure S16). Finally, the possible formation of an electrode-adsorbed active catalyst was excluded through a series of control experiments. First, peak currents for $[\mathbf{Fe1}]^{2+}$ and $[\mathbf{Zn1}]^{2+}$ scale linearly with the square root of the scan rate, indicative of freely diffusing species in solution (Figures S17 and S18). Second, CPE rinse tests[62] which probe for electrode deposition, give complete inversion of product selectivity, with H_2 as the predominant product and negligible generation of CO (Figure S19).

Kinetic Analysis of Electrochemical CO_2RR Catalyzed by [Fe(tpyPY2Me)]$^{2+}$ in Organic Solution. Encouraged by the high selectivity of $[\mathbf{Fe1}]^{2+}$ for electrochemical CO_2RR over competing HER processes, we sought to evaluate its kinetic performance. Cyclic voltammograms acquired for $[\mathbf{Fe1}]^{2+}$ under CO_2-saturated electrolyte in the presence of 3.5 M phenol (Figure S20) exhibit scan rate dependence and noncanonical peak-shaped waves, indicative of competitive, nonideal processes (e.g., substrate consumption, product inhibition, etc.). As a result, k_{obs} (TOF_{max}) obtained from catalytic plateau current analysis is not appropriate here and will lead to underestimations of the rates of CO_2 reduction.[63] Therefore, we instead extracted kinetic parameters directly from our variable potential CPE experiments (Figure S11), as described by Savéant and co-workers,[64,65] where the products (CO and H_2) were detected and quantified by gas chromatography (Figures S21 and S22). The observed rate constants (k_{obs}) at each applied potential were extracted from the averaged specific current density for CO production (j_{CO}) taken across the entire 1 h CPE experiments (Figure S11) that were conducted in triplicate (see Supporting Information for additional details).

A catalytic Tafel plot was constructed from our CPE experiments with direct product quantification (Figure 5b) and is summarized in Table S7. Tafel analysis identifies $[\mathbf{Fe1}]^{2+}$ as one of the most active molecular electrocatalysts reported to date with it achieving a turnover frequency (TOF) of 75,000 s^{-1} at an applied overpotential as low as 190 mV (−1.46 V vs Fc/

https://dx.doi.org/10.1021/jacs.0c10664
J. Am. Chem. Soc. 2020, 142, 20489−20501

Fc^+) and reaching TOFs > 500 000 s^{-1} between overpotentials of 560−710 mV (−1.81 and −1.98 V vs Fc/Fc^+) (Figure S23). Notably, this rapid, homogeneous CO_2 reduction catalysis is achieved without any modifications to the secondary coordination sphere to introduce hydrogen bond/proton-relay functionalities to break electronic scaling relationships.[13,14,47,66−69]

In parallel, we also attempted to apply foot-of-the-wave analysis (FOWA) as pioneered by Savéant[64,65] to estimate the kinetics based solely on CVs collected in the presence and absence of CO_2. FOWA estimates the idealized catalytic reactivity by considering the initial portion of the catalytic wave where the effects of side phenomena are expected to be minimal. Unfortunately, FOWA does not find clear application here because the linear region of the FOW is very small and is ill defined due to the appearance of a pre-wave feature at −1.36 V vs Fc/Fc^+ and a multi-segmented catalytic wave with apparent maxima at −1.56 and −1.96 V vs Fc/Fc^+ (Figures 4c and S24). The existence of this multi-segmented catalytic wave may suggest that the catalytic resting state is changing as more negative potentials are applied. Therefore, the extraction of kinetic data based on our CPE experiments results in more accurate analysis as they are determined from preparative scale experiments that directly detect and measure CO rather than relying on estimations of observed rate constants determined from CV data.

Finally, to assess the long-term catalytic stability and recyclability of $[\mathbf{Fe1}]^{2+}$, four consecutive 5 h CPE experiments were conducted at −1.98 V (versus Fc/Fc^+), the highest potential investigated, without addition of fresh $[\mathbf{Fe1}]^{2+}$ between each experiment (Figure S25). $[\mathbf{Fe1}]^{2+}$ is remarkably stable with 221 C of charge passed over the 20 h window without any loss in selectivity for CO (average FE_{CO} = 87%).

Chemical Reduction and Characterization of [Fe(tpyPY2Me)]^0 ([Fe1]^0). We reasoned that the observed electrocatalytic efficiency of $[\mathbf{Fe1}]^{2+}$ for CO_2RR stems from a synergistic effect between the iron center and the redox-active tpyPY2Me ligand, as both components are necessary to achieve selective CO_2RR reactivity. To establish a molecular-level framework for understanding this metal−ligand cooperativity, we sought to synthesize, isolate, and characterize the two-electron reduced complex, [Fe(tpyPY2Me)]^0 ($[\mathbf{Fe1}]^0$), which we hypothesize has putative catalytic relevance. Chemical reduction of $[\mathbf{Fe1}]^{2+}$ with 2.2 equiv of decamethylcobaltocene (Figure 6a) produced $[\mathbf{Fe1}]^0$ as a dark purple solid. Interestingly, room temperature ^{1}H NMR analysis of $[\mathbf{Fe1}]^0$ in CD_3CN revealed that the compound is diamagnetic with the aryl and aliphatic signals shifted upfield (Figure 6b). In support of this result, a nearly identical ^{1}H NMR spectrum was obtained for the product $[\mathbf{Zn1}]^0$ generated from the chemical reduction of $[\mathbf{Zn1}]^{2+}$ with potassium graphite (see Figure S26 and details in the Supporting Information). These data are consistent with our assignment of the reduction features for both $[\mathbf{Fe1}]^{2+}$ and $[\mathbf{Zn}]^{2+}$ as ligand-centered events. Frozen solution Fe K-edge X-ray absorption near-edge spectroscopy (XANES) was used to characterize metal oxidation states (Figure 7). Absorption edge energies were determined from the second derivative zero crossings, giving the following values (eV): 7126.9 ($[\mathbf{Fe1}]^0$) and 7127.4 ($[\mathbf{Fe1}]^{2+}$). These values are similar to compounds in the literature[70] leading to the assignment of the oxidation states of both species as Fe(II).

Given the unique diamagnetic ground state of $[\mathbf{Fe1}]^0$, two major electronic structures are possible. The first possibility is a low-spin iron(II) center (S_{Fe} = 0) coordinated to a reduced

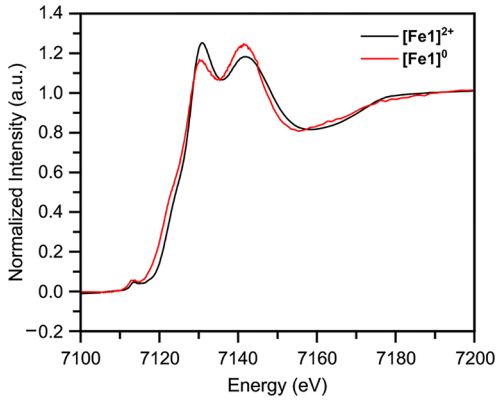

Figure 7. Experimental Fe K-edge XAS spectra of $[\mathbf{Fe1}]^{2+}$ (black) and two-electron reduced $[\mathbf{Fe1}]^0$ (red), supporting a formal Fe(II) oxidation state assignment for both species.

closed-shell singlet ligand ($S_{tpyPY2Me}$ = 0) generated by both electrons occupying the same π^* orbital (i.e., [Fe(tpyPY2Me)$^{2-}$]^0). The other possibility is an intermediate-spin iron(II) center (S_{Fe} = 1) antiferromagnetically coupled to a reduced ligand with an open-shell triplet configuration ($S_{tpyPY2Me}$ = 1) through half occupation of both low-lying π^* terpyridine orbitals, leading to an overall metal−ligand spin-coupled electronic structure (i.e., [Fe(tpyPY2Me$^{\bullet\bullet}$)$^{2-}$]^0). The two electronic configurations are more clearly distinguished here by specifying the spin state of the ligand as either a singlet (tpyPY2Me)$^{2-}$ or a triplet (tpyPY2Me$^{\bullet\bullet}$)$^{2-}$ in the chemical formula. Because of the large anodic shift (640 mV) in the ligand-based reductions of $[\mathbf{Fe1}]^{2+}$ relative to $[\mathbf{Zn1}]^{2+}$ (Figure 4a), the electrochemistry indicates a strong influence of the metal center and supports assignment to a [Fe(tpyPY2Me$^{\bullet\bullet}$)$^{2-}$]^0 electronic configuration. In further support of this model, Mössbauer data for $[\mathbf{Fe1}]^0$ revealed an isomer shift of δ = 0.2608(2) mm/s and a quadrupole splitting of $|\Delta E_Q|$ = 0.7637(4) mm/s, consistent with the formation of intermediate-spin iron(II) (Figures 6c and S27).[71] The antiferromagnetic coupling between the reduced biradical ligand, (tpyPY2Me$^{\bullet\bullet}$)$^{2-}$, and the intermediate-spin iron(II) is expected to be quite strong given that a diamagnetic ^{1}H NMR spectrum is observed at room temperature. Indeed, DFT calculations predict a large coupling constant of −1023 cm^{-1}, giving rise to a singlet-quintet gap of 4400 cm^{-1} (see the Supporting Information).

Further insights into the electronic structure of $[\mathbf{Fe1}]^0$ can be gleaned from the solid-state structure of $[\mathbf{Fe1}]^0$. Single crystals of $[\mathbf{Fe1}]^0$ were obtained by slow evaporation of a saturated acetonitrile solution, and X-ray diffraction analysis revealed a distorted square pyramidal geometry (Figure 6d; Tables S8 and S9) resulting from the loss of the axial acetonitrile ligand in $[\mathbf{Fe1}]^{2+}$. This structure is in good agreement with the reduction pathway predicted by DFT (*vide infra*). The bond metrics of the terpyridine moiety unambiguously supports the two-electron reduction of the tpyPY2Me ligand in the solid state and thus the iron(II) oxidation state assignment. In particular, the contraction of the intra-pyridine bond lengths (C_{py}−C'_{py}), from an average of 1.474(3) Å in $[\mathbf{Fe1}]^{2+}$ to 1.434(4) Å in $[\mathbf{Fe1}]^0$ is consistent with the metrics with which the oxidation levels of terpyridine can be established as determined through structural studies on a series of iron(II) and chromium(III) bis-terpyridine complexes reported by Wieghardt and co-workers.[72,73] Furthermore, average C−N bond lengths of the terpyridine

https://dx.doi.org/10.1021/jacs.0c10664
J. Am. Chem. Soc. 2020, 142, 20489−20501

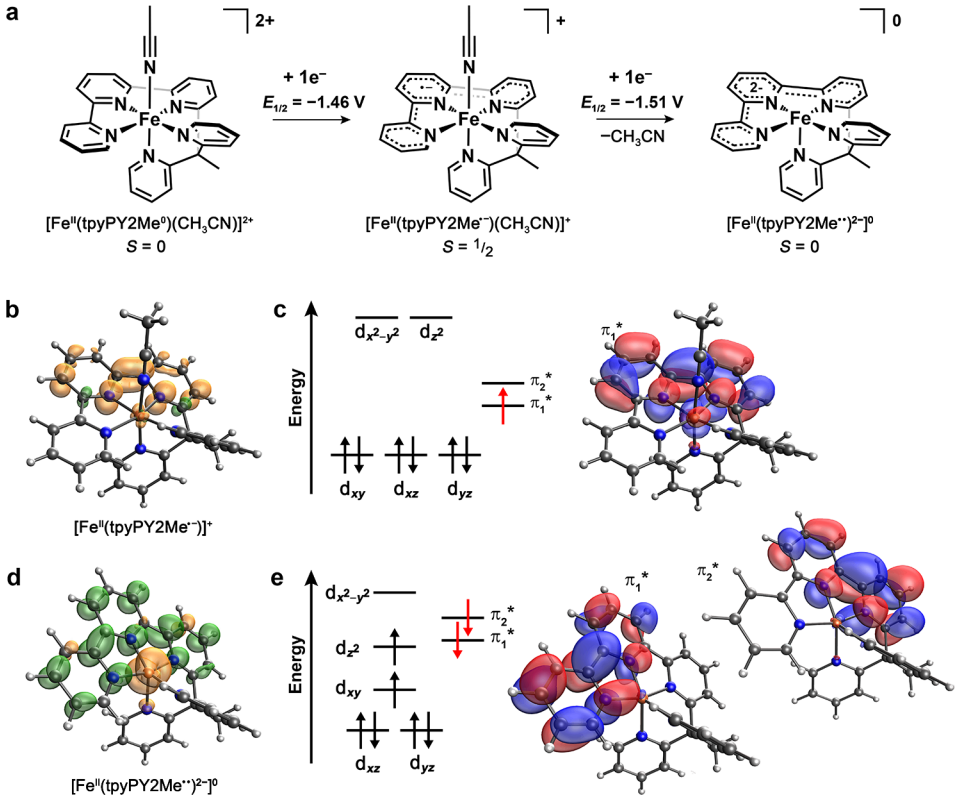

Figure 8. DFT analysis and calculated molecular orbitals for $[\mathbf{Fe1}]^{+}$ and $[\mathbf{Fe1}]^{0}$ species. (a) DFT predicted pathway for reduction of $[\mathbf{Fe1}]^{2+}$ to the open-shell singlet $[\mathbf{Fe1}]^{0}$, $[Fe(tpyPY2Me^{\bullet\bullet})^{2-}]^{0}$. The computed reduction potentials are given for reduction of $[\mathbf{Fe1}]^{2+}$ to $[\mathbf{Fe1}]^{+}$ and $[\mathbf{Fe1}]^{+}$ to $[\mathbf{Fe1}]^{0}$. See Table S11 for the predicted reduction pathways for $[\mathbf{Zn(1)}]^{2+/0}$ and for the closed-shell singlet $[\mathbf{Fe1}]^{0}$, $[Fe(tpyPY2Me)^{2-}]^{0}$. (b) Spin density plot and (c) simplified molecular orbital diagram of the one electron reduced intermediate $[\mathbf{Fe1}]^{+}$. (d) Spin density plot and (e) simplified molecular orbital diagram of $[\mathbf{Fe1}]^{0}$ ($[Fe(tpyPY2Me^{\bullet\bullet})^{2-}]^{0}$). Localized metal orbitals are depicted in the Supporting Information.

moiety in $[\mathbf{Fe1}]^{0}$ (1.384(3) Å) depart quite significantly from what would be expected for typical, neutral aromatic pyridine rings (1.35 ± 0.1 Å, respectively)[72] and what was observed in the solid state structure of $[\mathbf{Fe1}]^{2+}$ (1.353(2) Å).

Distinguishing between the two possible electronic configurations of $[\mathbf{Fe1}]^{0}$ based on the single crystal X-ray diffraction data is more challenging. The DFT predicted structure for the open-shell singlet ($[Fe(tpyPY2Me^{\bullet\bullet})^{2-}]^{0}$) more closely matches the experimental bond metrics of $[\mathbf{Fe1}]^{0}$ than does the predicted structure of the closed-shell singlet ($[Fe(tpyPY2Me)^{2-}]^{0}$); however the solid state structures are susceptible to additional packing and dispersion forces that are not accounted for by DFT calculations (Table S10). In theory, the unique bonding interactions of the two terpyridine LUMOs[72−74] should enable us to directly distinguish between the two possible electronic configurations of $[\mathbf{Fe1}]^{0}$, but the change in bond metrics between the dianionic, singlet ligand ($tpyPY2Me^{2-}$) and the triplet, π radical dianion ($tpyPY2Me^{\bullet\bullet 2-}$) is expected to be quite subtle given the metrics reported by Wieghardt and co-workers on a series of reduced homoleptic bis(terpyridine) complexes ($[M(tpy)_2]^{n+}$; M = Cr, Fe).[72,73] Attempts to crystallize $[\mathbf{Zn1}]^{0}$ have been unsuccessful to date, thus preventing direct crystallographic comparison to $[\mathbf{Fe1}]^{0}$.

Although absolute determination of the electronic structure should not be based solely on X-ray diffraction, when it is taken together with the electrochemical, NMR, and Mössbauer results, the collective data support the iron(II) oxidation state assignment of $[\mathbf{Fe1}]^{0}$ as an open-shell singlet ground state ($[Fe(tpyPY2Me^{\bullet\bullet})^{2-}]^{0}$) composed of an intermediate-spin iron(II) center (S_{Fe} = 1) that is antiferromagnetically coupled to a doubly reduced tpyPY2Me (S_{tpy} = 1) ligand. This strong exchange coupling shifts the tpyPY2Me-based reductions of $[\mathbf{Fe1}]^{2+}$ to more positive potentials relative to the analog with the redox-silent Zn(II) center by 640 mV, which we hypothesize ultimately promotes highly selective CO_2 reduction by $[\mathbf{Fe1}]^{2+}$. To further elucidate the electronic structures of $[\mathbf{Fe1}]^{2+/0}$, we subsequently applied extensive DFT and multireference methods.

Electronic Structure Calculations Support Strong Metal−Ligand Exchange Coupling Between Fe and tpyPY2Me Units. We carried out DFT calculations using the ωB97X-D functional to generate a more accurate molecular orbital picture of our $[\mathbf{Fe1}]^{2+}$ system. Optimized structures and predicted redox potentials for $[\mathbf{Fe1}]^{2+}$ and $[\mathbf{Zn1}]^{2+}$ are in good agreement with experimental data (Tables S11 and 12). Interestingly, although the DFT data indicate the metal center in $[\mathbf{Fe1}]^{2+}$ is best described as low-spin iron(II), the calculated singlet-quintet gap is small, explaining the observed thermal population of a higher spin-state at room temperature (Tables S13 and 14). The first reduction of $[\mathbf{Fe1}]^{2+}$ to $[\mathbf{Fe1}]^{+}$ is predicted to generate a ground state doublet composed of a low-spin iron(II) and a tpyPY2Me-based radical $(tpyPY2Me^{\bullet})^{1-}$ with a predicted redox potential of −1.46 V (Figure 8a−c). The spin density plot of this $[\mathbf{Fe1}]^{+}$ species indicates a ligand-based reduction with almost no excess spin on the iron center (Figure 8b). The second reduction populates a second low lying π^* orbital of tpyPY2Me and induces loss of the axial acetonitrile

https://dx.doi.org/10.1021/jacs.0c10664
J. Am. Chem. Soc. 2020, 142, 20489−20501

molecule, providing access to an intermediate-spin iron(II) state (Figure 8a,d,e). The S_{Fe} = 1 iron center is strongly antiferromagnetically coupled to the two electrons in the tpyPY2Me π^* orbitals (i.e., $[Fe(tpyPY2Me^{\bullet\bullet})^{2-}]^0$; Figure 8e). Localized orbital bonding analysis confirmed that iron remains in the 2^+ oxidation state during the second reduction process, which has a predicted reduction potential of −1.51 V. This predicted redox potential is in good agreement with that observed experimentally.

In contrast, the other feasible closed-shell singlet configuration: a low-spin iron(II) center (S_{Fe} = 0) coordinated to a reduced closed-shell doubly reduced singlet ligand ($S_{tpyPY2Me}$ = 0) (i.e., $[Fe(tpyPY2Me)^{2-}]^0$), does not match the experimental data. The doubly reduced tpy ligand is strongly π basic and thus delocalizes some electron density into the empty metal orbitals (distorted e_g-type). The computed reduction potential of −2.03 V vs Fc/Fc^+ using the $[Fe(tpyPY2Me)^{2-}]^0$ electronic configuration does not match the experimental value of −1.43 V vs Fc/Fc^+. This difference can be rationalized by the large free energy gap (12 kcal/mol) between the broken symmetry solution ($[Fe(tpyPY2Me^{\bullet\bullet})^{2-}]^0$) and the closed-shell singlet ($[Fe(tpyPY2Me)^{2-}]^0$) consisting of low-spin iron(II) (S_{Fe} = 0) and doubly reduced ligand ($S_{tpyPY2Me}$ = 0) (Tables S13 and 14). It should also be noted that a large variety of different hybrid density functionals all predict the broken symmetry configuration as the ground state on the singlet surface (see Table S14).

In addition, multi-reference calculations using complete active space self-consistent field (CASSCF) confirmed the antiferromagnetically coupled ground state (see the Supporting Information). This calculation reveals a strong entanglement of the two ligand-based orbitals and the two metal d-orbitals. In particular, the axial distortion away from octahedral symmetry allows the d_{z^2} and d_{xy} metal orbitals (or superposition of the two orbitals) to interact with the two tpyPY2Me π^* orbitals in a weak π-type interaction (Figure S28). Hence, the novel ligand framework with two low-lying π^* orbitals, a distorted coordination geometry, and a moderate ligand field in combination with the iron metal center stabilizes two excess electrons effectively. The spin transition alters both the energetics of the d-orbitals and local spin on the central metal to facilitate an effective antiferromagnetic coupling. In contrast, in the alternative closed-shell singlet electronic configuration ($[Fe(tpyPY2Me)^{2-}]^0$; S_{Fe} = 0 and S_{tpy} = 0), the stabilization of the doubly reduced tpyPY2Me π^* (S_{tpy} = 0) by the high lying e_g^* of the low-spin iron(II) (S_{Fe} = 0) is marginal. This feature is illustrated by the almost identical second ligand reduction potentials of $[\mathbf{Zn1}]^{2+}$ and $[\mathbf{Fe1}]^{2+}$ with a closed-shell singlet electronic structure (−2.02 V for $[\mathbf{Zn1}]^{2+}$ and −2.03 V vs Fc/Fc^+ for $[\mathbf{Fe1}]^{2+}$ with S_{Fe} = 0 and S_{tpy} = 0).

We note that a similar electronic structure involving this intramolecular antiferromagnetic coupling was proposed by Neese and co-workers for the electronic structure of another CO_2 reduction catalyst, the doubly reduced iron tetraphenylporphryin complex, $[Fe(TPP)]^{2-}$.[75] Through quantum mechanical calculations and spectroscopic data (Mössbauer and XAS) they assign both reductions of $[FeTPP]^{2-}$ to the porphyrin ligand framework and show that it is coupled to an intermediate-spin iron center (S_{Fe} = 1) giving an overall singlet state.[75] It should be noted that the iron center in the un-reduced iron(II) complex, $[Fe(TPP)]^0$, is intermediate-spin and therefore the metal center does not undergo a spin transition upon reduction. This behavior can be contrasted to the group VII CO_2 reduction catalyst, $[Re(bpy)(CO)_3]^-$ (and its Mn derivative), where the quantum chemical calculations and spectroscopic data revealed that one electron is placed into the π^* orbital of the non-innocent bpy ligand and the second electron is placed in the metal d_{z^2} orbital but is strongly delocalized into the three carbonyl ligands. Both electrons form a metal−ligand bond (delocalized metal−ligand orbital) with a singlet ground state which is 15 kcal/mol lower in energy than the uncoupled triplet state.[32] Thus, the "initial" d-orbitals are not involved in the stabilization of the excess electrons as they are in $[\mathbf{Fe1}]^{2+}$ and [Fe(TPP)].

Electrochemical CO_2RR Catalyzed by [Fe-(tpyPY2Me)]$^{2+}$ in Water. Given the low overpotentials required for $[\mathbf{Fe1}]^{2+}$ to catalyze homogeneous electrochemical CO_2 reduction in organic solvent, we sought to evaluate its activity in water (Figure 9). For this purpose, we prepared the more water-soluble nitrate analog of $[\mathbf{Fe1}]^{2+}$ (see the Supporting Information), and X-ray diffraction analysis revealed that anion exchange does not alter the catalyst structure (Figure S29; Tables S15 and S16). As a cheap, abundant, and benign solvent and proton source, water is an attractive medium for CO_2 reduction. However, homogeneous molecular CO_2

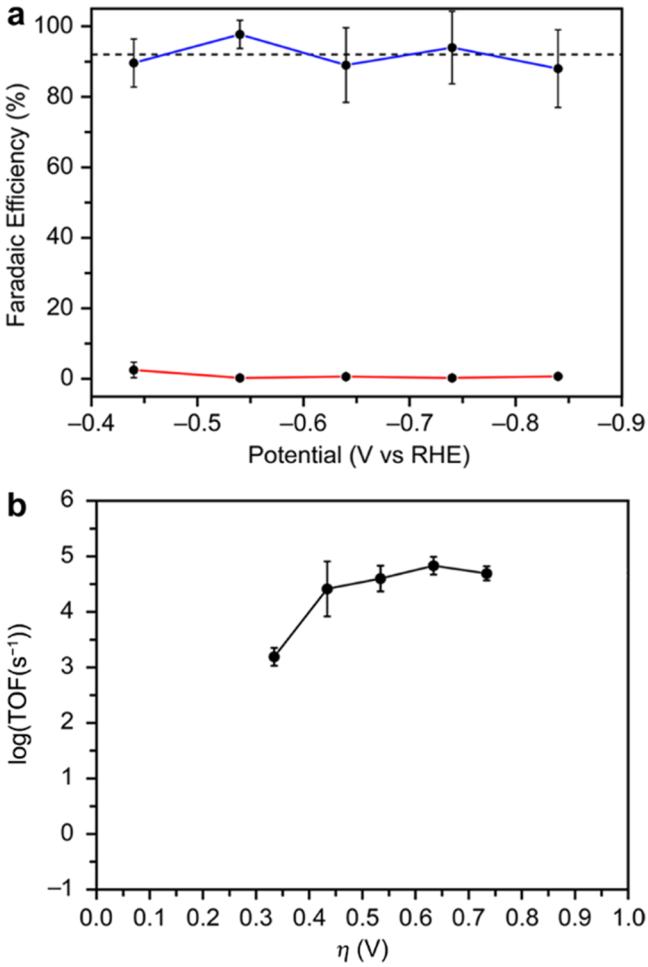

Figure 9. Aqueous CO_2 reduction performance for the Fe-tpyPY2Me electrocatalyst. (a) Faradaic efficiencies for CO (blue) and H_2 (red) formation at varying applied potentials for 60 min (averages of three experiments). The average FE_{CO} is indicated by the black dashed line. (b) Catalytic Tafel plot for $[\mathbf{Fe1}]^{2+}$ obtained from CPE experiments in 0.10 M $NaHCO_3$.

https://dx.doi.org/10.1021/jacs.0c10664
J. Am. Chem. Soc. 2020, 142, 20489−20501

reduction catalysts typically require mercury working electrodes to operate effectively in aqueous electrolytes because their onset potentials are too negative to be compatible with more desirable carbon-based electrodes that preferentially catalyze competing water reduction.[10,76−79] Owing to the 640 mV positive shift in 2-electron reduction potential upon moving from Zn(II) to Fe(II), we envisioned that CO_2RR could be favored over HER, even with water as both a solvent and proton source.

Against this backdrop, we were pleased to observe that cyclic voltammograms collected for $[\mathbf{Fe1}]^{2+}$ dissolved in 0.10 M $NaHCO_3$ with a carbon paste working electrode show the formation of a catalytic wave when saturated with CO_2 (Figure S30). Notably, variable potential CPE experiments (Figures S31−S35) revealed that $[\mathbf{Fe1}]^{2+}$ maintains its activity and selectivity for CO_2 reduction to CO in water (average FE_{CO} = 92% and FE_{H_2} < 1%) with maximum turnover frequencies, determined from direct product detection, reaching >50 000 s^{-1} at overpotentials of 500 mV (Figure 9b). Importantly, control rinse tests passed negligible current during 1 h CPE experiments, and the selectivity was inverted such that H_2 is the major product (Figures S31−S36). UV−visible spectra collected before and after electrolysis are nearly indistinguishable; however, cyclic voltammograms change quite drastically following the 1 h CPE (Figure S37) indicative of some degree of catalyst deposition and decomposition on the glassy carbon electrode. In line with this observation, electrochemical stripping behavior is also observed, which may contribute to slower catalysis in water relative to organic solvent (Figure S38). Nevertheless, these data show that $[\mathbf{Fe1}]^{2+}$ is an effective molecular catalyst for homogeneous CO_2 reduction in water. Crucially, given its molecular nature, the activity, stability, and overpotential of this catalyst can in principle be tuned through ligand modifications accessible by synthetic chemistry. Further, the study of this catalyst and related systems has the potential to shed important insights on the behavior of materials catalysts bearing atomically dispersed iron sites.[80]

CONCLUDING REMARKS

In summary, inspired by the beneficial feature of electronic delocalization exhibited by biological and heterogeneous systems for electrochemical CO_2RR catalysis to minimize overpotentials and favor CO_2RR over competing HER pathways, even in aqueous media, we report a molecular system that captures this design concept. A new ligand framework that incorporates a redox-active terpyridine moiety into a modular polypyridyl scaffold can achieve highly selective and efficient iron-catalyzed electrochemical CO_2 reduction to CO in both organic and aqueous solutions with high specificity over competing hydrogen evolution pathways. Importantly, the combination of both an open-shell metal ion using an earth-abundant, first-row transition metal in conjunction with a redox non-innocent ligand enables metal-cooperativity through strong exchange coupling that shifts electrochemical reduction potentials to promote CO_2RR catalysis. Specifically, the Fe(II) tpyPYMe2 analog exhibits a 640 mV positive shift in the 2-electron reduction potential relative to the isostructural analog bearing a redox-silent Zn(II) center, poising it for multielectron electrocatalysis with minimized overpotentials. Control experiments with Fe(II) and Zn(II) complexes bearing a related pentapyridine ligand lacking the redox-active terpyridine fragment and the same redox non-innocent ligand but with a redox-silent Zn(II) center show that CO_2RR relies on synergistic coupling between both metal and ligand components.

The combination of distorted coordination geometry, low-lying π^* orbitals, and moderate ligand field engendered by the rigid, redox non-innocent tpyPY2Me ligand promotes strong metal−ligand cooperativity with the iron(II) center. $[\mathbf{Fe1}]^{2+}$ is shown to catalyze CO_2 reduction at extremely mild redox potentials (η = 190 mV; − 1.46 V vs Fc/Fc^+) relative to the control polypyridyl complexes presented in this study. The positive redox potentials at which CO_2RR catalysis occurs is interpreted through extensive experimental spectroscopic (NMR, Mössbauer, and XAS), XRD, and electrochemical studies, along with electronic structure calculations, which collectively point to a model in which the two-electron reduced iron complex, $[\mathbf{Fe1}]^0$, possesses an open-shell singlet ground state electronic structure ($[Fe(tpyPY2Me^{\bullet\bullet})^{2-}]^0$) resulting from a strong intramolecular antiferromagnetic coupling between a triplet reduced ligand (tpyPY2Me tpyPY2Me$^{\bullet\bullet 2-}$; $S_{tpyPY2Me}$ = 1) and an intermediate-spin Fe(II) center (S_{Fe} = 1). We propose that the multielectron chemistry of $[\mathbf{Fe1}]^{2+}$ at relatively positive potentials is facilitated through this electronic structure, which in turn promotes its exceptional selectivity (FE_{CO} > 90%) through suppression of HER pathways. Furthermore, variable potential CPE experiments with direct product detection show that $[\mathbf{Fe1}]^{2+}$ operates at fast rates in both organic (TOF > 100 000 s^{-1}) and aqueous electrolytes (TOF > 50 000 s^{-1}) with robust long-term stability and recyclability.

The ability to create molecular compounds with strong exchange coupling between synergistic, redox non-innocent ligands and metal centers has broad implications for catalyst design, including enabling control over the density and arrangement of functional active sites. Indeed, redox balancing through electronic delocalization is pivotal for biological and materials catalysts to achieve complex chemical transformations at or near thermodynamic potentials. However, discrete molecular compounds offer a level of tunability via coordination chemistry that remains unparalleled in protein design and nanostructure engineering. Thus, inorganic molecules are uniquely positioned to open access to a range of new properties and offer a desirable alternative strategy for lowering energy barriers for redox catalysis. The observed 640 mV electrochemical potential shift and associated turn-on of CO_2RR catalysis upon substituting Zn(II) for Fe(II) for the same redox non-innocent ligand emphasizes metal−ligand cooperativity for redox balancing that goes beyond redox activity dominated at either ligand or metal sites alone.

ASSOCIATED CONTENT

Supporting Information

The Supporting Information is available free of charge at https://pubs.acs.org/doi/10.1021/jacs.0c10664.

X-ray crystallographic data for $[\mathbf{Fe1}]^{2+}$, $[\mathbf{Zn1}]^{2+}$, $[\mathbf{Fe1}]^0$, and $[Fe(tpyPY2Me)(NO_3)][NO_3]$ (CIF)

Experimental and computational details, compound characterization, supplemental electrochemical and spectroscopic data, and DFT geometry optimized atomic xyz coordinates (PDF)

https://dx.doi.org/10.1021/jacs.0c10664
J. Am. Chem. Soc. 2020, 142, 20489−20501

AUTHOR INFORMATION

Corresponding Author

Christopher J. Chang − *Department of Chemistry and Department of Molecular and Cell Biology, University of California, Berkeley, California 94720, United States; Chemical Sciences Division, Lawrence Berkeley National Laboratory, Berkeley, California 94720, United States;* orcid.org/0000-0001-5732-9497; Email: chrischang@berkeley.edu

Authors

Jeffrey S. Derrick − *Department of Chemistry, University of California, Berkeley, California 94720, United States; Chemical Sciences Division, Lawrence Berkeley National Laboratory, Berkeley, California 94720, United States*

Matthias Loipersberger − *Department of Chemistry, University of California, Berkeley, California 94720, United States;* orcid.org/0000-0002-3648-0101

Ruchira Chatterjee − *Molecular Biophysics and Integrated Bioimaging Division, Lawrence Berkeley National Laboratory, Berkeley, California 94720, United States*

Diana A. Iovan − *Department of Chemistry, University of California, Berkeley, California 94720, United States;* orcid.org/0000-0001-9889-7183

Peter T. Smith − *Department of Chemistry, University of California, Berkeley, California 94720, United States; Chemical Sciences Division, Lawrence Berkeley National Laboratory, Berkeley, California 94720, United States*

Khetpakorn Chakarawet − *Department of Chemistry, University of California, Berkeley, California 94720, United States;* orcid.org/0000-0001-5905-3578

Junko Yano − *Molecular Biophysics and Integrated Bioimaging Division, Lawrence Berkeley National Laboratory, Berkeley, California 94720, United States;* orcid.org/0000-0001-6308-9071

Jeffrey R. Long − *Department of Chemistry and Department of Chemical and Biomolecular Engineering, University of California, Berkeley, California 94720, United States; Materials Sciences Division, Lawrence Berkeley National Laboratory, Berkeley, California 94720, United States;* orcid.org/0000-0002-5324-1321

Martin Head-Gordon − *Department of Chemistry, University of California, Berkeley, California 94720, United States; Chemical Sciences Division, Lawrence Berkeley National Laboratory, Berkeley, California 94720, United States;* orcid.org/0000-0002-4309-6669

Complete contact information is available at: https://pubs.acs.org/10.1021/jacs.0c10664

Notes

The authors declare no competing financial interest.

ACKNOWLEDGMENTS

This research was supported by the Director, Office of Science, Office of Basic Energy Sciences, and the Division of Chemical Sciences, Geosciences, and Bioscience of the U.S. Department of Energy at Lawrence Berkeley National Laboratory (Grant No. DE-AC02-05CH11231 to C.J.C.; Grant No. DE-AC02-05CH11231 to J.Y.), and the U.S. Department of Energy, Office of Science, Office of Advanced Scientific Computing, and the Office of Basic Energy Sciences via the Scientific Discovery through Advanced Computing (SciDAC) program (to M.H-G), Collection and interpretation of Mössbauer spectra were supported by National Science Foundation CHE-1800252 to J.R.L. C.J.C. is a CIFAR Fellow. P.T.S. acknowledges the NSF for a graduate research fellowship. We thank Dr. Hasan Celik and UC Berkeley's NMR facility in the College of Chemistry (CoC-NMR) and Dr. Ping Yu and UC Davis's NMR facility for spectroscopic assistance. Instruments in the CoC-NMR are supported in part by NIH S10OD024998. We thank Dr. N. Settineri for assistance with X-ray crystallography. We thank R. Murphy, C. Gould, C. Stein, and Dr. A. Wuttig for fruitful discussions and Dr. K. R. Meihaus for editorial assistance. We dedicate this manuscript to Prof. Dick Andersen.

REFERENCES

(1) Lewis, N. S.; Nocera, D. G. Powering the Planet: Chemical Challenges in Solar Energy Utilization. *Proc. Natl. Acad. Sci. U. S. A.* **2006**, *103* (43), 15729−15735.

(2) De Luna, P.; Hahn, C.; Higgins, D.; Jaffer, S. A.; Jaramillo, T. F.; Sargent, E. H. What Would It Take for Renewably Powered Electrosynthesis to Displace Petrochemical Processes? *Science* **2019**, *364* (6438), 3506.

(3) Francke, R.; Schille, B.; Roemelt, M. Homogeneously Catalyzed Electroreduction of Carbon Dioxide—Methods, Mechanisms, and Catalysts. *Chem. Rev.* **2018**, *118* (9), 4631−4701.

(4) Can, M.; Armstrong, F. A.; Ragsdale, S. W. Structure, Function, and Mechanism of the Nickel Metalloenzymes, CO Dehydrogenase, and Acetyl-CoA Synthase. *Chem. Rev.* **2014**, *114* (8), 4149−4174.

(5) Corbin, N.; Zeng, J.; Williams, K.; Manthiram, K. Heterogeneous Molecular Catalysts for Electrocatalytic CO_2 Reduction. *Nano Res.* **2019**, *12* (9), 2093−2125.

(6) Smith, P. T.; Nichols, E. M.; Cao, Z.; Chang, C. J. Hybrid Catalysts for Artificial Photosynthesis: Merging Approaches from Molecular, Materials, and Biological Catalysis. *Acc. Chem. Res.* **2020**, *53* (3), 575−587.

(7) Fisher, B. J.; Eisenberg, R. Electrocatalytic Reduction of Carbon Dioxide by Using Macrocycles of Nickel and Cobalt. *J. Am. Chem. Soc.* **1980**, *102* (24), 7361−7363.

(8) Beley, M.; Collin, J.-P.; Ruppert, R.; Sauvage, J.-P. Nickel(II)-Cyclam: An Extremely Selective Electrocatalyst for Reduction of CO_2 in Water. *J. Chem. Soc., Chem. Commun.* **1984**, *19*, 1315−1316.

(9) Schneider, J.; Jia, H.; Kobiro, K.; Cabelli, D. E.; Muckerman, J. T.; Fujita, E. Nickel(II) Macrocycles: Highly Efficient Electrocatalysts for the Selective Reduction of CO_2 to CO. *Energy Environ. Sci.* **2012**, *5* (11), 9502−9510.

(10) Froehlich, J. D.; Kubiak, C. P. Homogeneous CO_2 Reduction by Ni(Cyclam) at a Glassy Carbon Electrode. *Inorg. Chem.* **2012**, *51* (7), 3932−3934.

(11) Hammouche, M.; Lexa, D.; Savéant, J. M.; Momenteau, M. Catalysis of the Electrochemical Reduction of Carbon Dioxide by Iron("0") Porphyrins. *J. Electroanal. Chem.* **1988**, *249* (1), 347−351.

(12) Meshitsuka, S.; Ichikawa, M.; Tamaru, K. Electrocatalysis by Metal Phthalocyanines in the Reduction of Carbon Dioxide. *J. Chem. Soc., Chem. Commun.* **1974**, No. 5, 158−159.

(13) Costentin, C.; Drouet, S.; Robert, M.; Savéant, J.-M. A Local Proton Source Enhances CO_2 Electroreduction to CO by a Molecular Fe Catalyst. *Science* **2012**, *338* (6103), 90−94.

(14) Azcarate, I.; Costentin, C.; Robert, M.; Savéant, J.-M. Through-Space Charge Interaction Substituent Effects in Molecular Catalysis Leading to the Design of the Most Efficient Catalyst of CO_2-to-CO Electrochemical Conversion. *J. Am. Chem. Soc.* **2016**, *138* (51), 16639−16644.

(15) Ren, S.; Joulié, D.; Salvatore, D.; Torbensen, K.; Wang, M.; Robert, M.; Berlinguette, C. P. Molecular Electrocatalysts Can Mediate Fast, Selective CO_2 Reduction in a Flow Cell. *Science* **2019**, *365* (6451), 367−369.

(16) Hawecker, J.; Lehn, J.-M.; Ziessel, R. Electrocatalytic Reduction of Carbon Dioxide Mediated by $Re(bipy)(CO)_3Cl$ (bipy = 2,2'-Bipyridine). *J. Chem. Soc., Chem. Commun.* **1984**, 328−330.

(17) Smieja, J. M.; Kubiak, C. P. Re(bipy-tBu)$(CO)_3$Cl-improved Catalytic Activity for Reduction of Carbon Dioxide: IR-Spectroelectrochemical and Mechanistic Studies. *Inorg. Chem.* **2010**, *49* (20), 9283−9289.
(18) Reda, T.; Plugge, C. M.; Abram, N. J.; Hirst, J. Reversible Interconversion of Carbon Dioxide and Formate by an Electroactive Enzyme. *Proc. Natl. Acad. Sci. U. S. A.* **2008**, *105* (31), 10654−10658.
(19) Evans, R. M.; Siritanaratkul, B.; Megarity, C. F.; Pandey, K.; Esterle, T. F.; Badiani, S.; Armstrong, F. A. The Value of Enzymes in Solar Fuels Research - Efficient Electrocatalysts through Evolution. *Chem. Soc. Rev.* **2019**, *48* (7), 2039−2052.
(20) Nitopi, S.; Bertheussen, E.; Scott, S. B.; Liu, X.; Engstfeld, A. K.; Horch, S.; Seger, B.; Stephens, I. E. L.; Chan, K.; Hahn, C.; Nørskov, J. K.; Jaramillo, T. F.; Chorkendorff, I. Progress and Perspectives of Electrochemical CO_2 Reduction on Copper in Aqueous Electrolyte. *Chem. Rev.* **2019**, *119* (12), 7610−7672.
(21) Todorova, T. K.; Schreiber, M. W.; Fontecave, M. Mechanistic Understanding of CO_2 Reduction Reaction (CO2RR) Toward Multicarbon Products by Heterogeneous Copper-Based Catalysts. *ACS Catal.* **2020**, *10* (3), 1754−1768.
(22) Rodriguez, P.; Koper, M. T. M. Electrocatalysis on Gold. *Phys. Chem. Chem. Phys.* **2014**, *16* (27), 13583−13594.
(23) Karunadasa, H. I.; Chang, C. J.; Long, J. R. A Molecular Molybdenum-Oxo Catalyst for Generating Hydrogen from Water. *Nature* **2010**, *464* (7293), 1329−1333.
(24) Karunadasa, H. I.; Montalvo, E.; Sun, Y.; Majda, M.; Long, J. R.; Chang, C. J. A Molecular MoS_2 Edge Site Mimic for Catalytic Hydrogen Generation. *Science* **2012**, *335* (6069), 698−702.
(25) Zee, D. Z.; Chantarojsiri, T.; Long, J. R.; Chang, C. J. Metal-Polypyridyl Catalysts for Electro- and Photochemical Reduction of Water to Hydrogen. *Acc. Chem. Res.* **2015**, *48* (7), 2027−2036.
(26) Sun, Y.; Bigi, J. P.; Piro, N. A.; Tang, M. L.; Long, J. R.; Chang, C. J. Molecular Cobalt Pentapyridine Catalysts for Generating Hydrogen from Water. *J. Am. Chem. Soc.* **2011**, *133* (24), 9212−9215.
(27) Chen, Z.; Chen, C.; Weinberg, D. R.; Kang, P.; Concepcion, J. J.; Harrison, D. P.; Brookhart, M. S.; Meyer, T. J. Electrocatalytic Reduction of CO_2 to CO by Polypyridyl Ruthenium Complexes. *Chem. Commun.* **2011**, *47* (47), 12607−12609.
(28) Gonell, S.; Massey, M. D.; Moseley, I. P.; Schauer, C. K.; Muckerman, J. T.; Miller, A. J. M. The *Trans* Effect in Electrocatalytic CO_2 Reduction: Mechanistic Studies of Asymmetric Ruthenium Pyridyl-Carbene Catalysts. *J. Am. Chem. Soc.* **2019**, *141* (16), 6658−6671.
(29) Gonell, S.; Assaf, E. A.; Duffee, K. D.; Schauer, C. K.; Miller, A. J. M. Kinetics of the *Trans* Effect in Ruthenium Complexes Provide Insight into the Factors That Control Activity and Stability in CO_2 Electroreduction. *J. Am. Chem. Soc.* **2020**, *142* (19), 8980−8999.
(30) Li, T.-T.; Shan, B.; Xu, W.; Meyer, T. J. Electrocatalytic CO_2 Reduction with a Ruthenium Catalyst in Solution and on Nanocrystalline TiO_2. *ChemSusChem* **2019**, *12* (11), 2402−2408.
(31) Liu, Y.; Fan, X.; Nayak, A.; Wang, Y.; Shan, B.; Quan, X.; Meyer, T. J. Steering CO_2 Electroreduction toward Ethanol Production by a Surface-Bound Ru Polypyridyl Carbene Catalyst on N-Doped Porous Carbon. *Proc. Natl. Acad. Sci. U. S. A.* **2019**, *116* (52), 26353−26358.
(32) Benson, E. E.; Sampson, M. D.; Grice, K. A.; Smieja, J. M.; Froehlich, J. D.; Friebel, D.; Keith, J. A.; Carter, E. A.; Nilsson, A.; Kubiak, C. P. The Electronic States of Rhenium Bipyridyl Electrocatalysts for CO_2 Reduction as Revealed by X-Ray Absorption Spectroscopy and Computational Quantum Chemistry. *Angew. Chem., Int. Ed.* **2013**, *52* (18), 4841−4844.
(33) Clark, M. L.; Cheung, P. L.; Lessio, M.; Carter, E. A.; Kubiak, C. P. Kinetic and Mechanistic Effects of Bipyridine (bpy) Substituent, Labile Ligand, and Brønsted Acid on Electrocatalytic CO_2 Reduction by Re(bpy) Complexes. *ACS Catal.* **2018**, *8* (3), 2021−2029.
(34) Keith, J. A.; Grice, K. A.; Kubiak, C. P.; Carter, E. A. Elucidation of the Selectivity of Proton-Dependent Electrocatalytic CO_2 Reduction by *Fac*-Re(bpy)$(CO)_3$Cl. *J. Am. Chem. Soc.* **2013**, *135* (42), 15823−15829.
(35) Su, X.; McCardle, K. M.; Panetier, J. A.; Jurss, J. W. Electrocatalytic CO_2 Reduction with Nickel Complexes Supported by Tunable Bipyridyl-N-Heterocyclic Carbene Donors: Understanding Redox-Active Macrocycles. *Chem. Commun.* **2018**, *54* (27), 3351−3354.
(36) Su, X.; McCardle, K. M.; Chen, L.; Panetier, J. A.; Jurss, J. W. Robust and Selective Cobalt Catalysts Bearing Redox-Active Bipyridyl-N-Heterocyclic Carbene Frameworks for Electrochemical CO_2 Reduction in Aqueous Solutions. *ACS Catal.* **2019**, *9* (8), 7398−7408.
(37) Lin, S.; Diercks, C. S.; Zhang, Y.-B.; Kornienko, N.; Nichols, E. M.; Zhao, Y.; Paris, A. R.; Kim, D.; Yang, P.; Yaghi, O. M.; Chang, C. J. Covalent Organic Frameworks Comprising Cobalt Porphyrins for Catalytic CO_2 Reduction in Water. *Science* **2015**, *349* (6253), 1208−1213.
(38) Diercks, C. S.; Lin, S.; Kornienko, N.; Kapustin, E. A.; Nichols, E. M.; Zhu, C.; Zhao, Y.; Chang, C. J.; Yaghi, O. M. Reticular Electronic Tuning of Porphyrin Active Sites in Covalent Organic Frameworks for Electrocatalytic Carbon Dioxide Reduction. *J. Am. Chem. Soc.* **2018**, *140* (3), 1116−1122.
(39) Gonell, S.; Lloret-Fillol, J.; Miller, A. An Iron Pyridyl-Carbene Catalyst for Low Overpotential CO_2 Reduction to CO: Mechanistic Comparisons with the Ruthenium Analogue and Photochemical Promotion. *ChemRxiv Preprint* **2020**, 11911383.
(40) Eisenberg, R.; Gray, H. B. Noninnocence in Metal Complexes: A Dithiolene Dawn. *Inorg. Chem.* **2011**, *50* (20), 9741−9751.
(41) McNamara, W. R.; Han, Z.; Alperin, P. J.; Brennessel, W. W.; Holland, P. L.; Eisenberg, R. A Cobalt-Dithiolene Complex for the Photocatalytic and Electrocatalytic Reduction of Protons. *J. Am. Chem. Soc.* **2011**, *133* (39), 15368−15371.
(42) McNamara, W. R.; Han, Z.; Yin, C.-J.; Brennessel, W. W.; Holland, P. L.; Eisenberg, R. Cobalt-Dithiolene Complexes for the Photocatalytic and Electrocatalytic Reduction of Protons in Aqueous Solutions. *Proc. Natl. Acad. Sci. U. S. A.* **2012**, *109* (39), 15594−15599.
(43) Letko, C. S.; Panetier, J. A.; Head-Gordon, M.; Tilley, T. D. Mechanism of the Electrocatalytic Reduction of Protons with Diaryldithiolene Cobalt Complexes. *J. Am. Chem. Soc.* **2014**, *136* (26), 9364−9376.
(44) Wu, Y.; Jiang, J.; Weng, Z.; Wang, M.; Broere, D. L. J.; Zhong, Y.; Brudvig, G. W.; Feng, Z.; Wang, H. Electroreduction of CO_2 Catalyzed by a Heterogenized Zn-Porphyrin Complex with a Redox-Innocent Metal Center. *ACS Cent. Sci.* **2017**, *3* (8), 847−852.
(45) Proppe, A. H.; Li, Y. C.; Aspuru-Guzik, A.; Berlinguette, C. P.; Chang, C. J.; Cogdell, R.; Doyle, A. G.; Flick, J.; Gabor, N. M.; van Grondelle, R.; Hammes-Schiffer, S.; Jaffer, S. A.; Kelley, S. O.; Leclerc, M.; Leo, K.; Mallouk, T. E.; Narang, P.; Schlau-Cohen, G. S.; Scholes, G. D.; Vojvodic, A.; Yam, V. W.-W.; Yang, J. Y.; Sargent, E. H. Bioinspiration in Light Harvesting and Catalysis. *Nat. Rev. Mater.* **2020**, *5*, 828.
(46) Jurss, J. W.; Khnayzer, R. S.; Panetier, J. A.; El Roz, K. A.; Nichols, E. M.; Head-Gordon, M.; Long, J. R.; Castellano, F. N.; Chang, C. J. Bioinspired Design of Redox-Active Ligands for Multielectron Catalysis: Effects of Positioning Pyrazine Reservoirs on Cobalt for Electro- and Photocatalytic Generation of Hydrogen from Water. *Chem. Sci.* **2015**, *6* (8), 4954−4972.
(47) Nichols, E. M.; Derrick, J. S.; Nistanaki, S. K.; Smith, P. T.; Chang, C. J. Positional Effects of Second-Sphere Amide Pendants on Electrochemical CO_2 Reduction Catalyzed by Iron Porphyrins. *Chem. Sci.* **2018**, *9* (11), 2952−2960.
(48) Smith, P. T.; Weng, S.; Chang, C. J. An NADH-Inspired Redox Mediator Strategy to Promote Second-Sphere Electron and Proton Transfer for Cooperative Electrochemical CO_2 Reduction Catalyzed by Iron Porphyrin. *Inorg. Chem.* **2020**, *59* (13), 9270−9278.
(49) Dey, S.; Das, P. K.; Dey, A. Mononuclear Iron Hydrogenase. *Coord. Chem. Rev.* **2013**, *257* (1), 42−63.
(50) Chantarojsiri, T.; Sun, Y.; Long, J. R.; Chang, C. J. Water-Soluble Iron(IV)-Oxo Complexes Supported by Pentapyridine Ligands: Axial Ligand Effects on Hydrogen Atom and Oxygen Atom Transfer Reactivity. *Inorg. Chem.* **2015**, *54* (12), 5879−5887.

https://dx.doi.org/10.1021/jacs.0c10664
J. Am. Chem. Soc. 2020, 142, 20489−20501

(51) Römelt, M.; Ye, S.; Neese, F. Calibration of Modern Density Functional Theory Methods for the Prediction of ^{57}Fe Mössbauer Isomer Shifts: Meta-GGA and Double-Hybrid Functionals. *Inorg. Chem.* **2009**, *48* (3), 784−785.
(52) McWilliams, S. F.; Brennan-Wydra, E.; MacLeod, K. C.; Holland, P. L. Density Functional Calculations for Prediction of ^{57}Fe Mössbauer Isomer Shifts and Quadrupole Splittings in β-Diketiminate Complexes. *ACS Omega* **2017**, *2* (6), 2594−2606.
(53) Pegis, M. L.; Roberts, J. A. S.; Wasylenko, D. J.; Mader, E. A.; Appel, A. M.; Mayer, J. M. Standard Reduction Potentials for Oxygen and Carbon Dioxide Couples in Acetonitrile and *N*,*N*-Dimethylformamide. *Inorg. Chem.* **2015**, *54* (24), 11883−11888.
(54) Matsubara, Y.; Grills, D. C.; Kuwahara, Y. Thermodynamic Aspects of Electrocatalytic CO_2 Reduction in Acetonitrile and with an Ionic Liquid as Solvent or Electrolyte. *ACS Catal.* **2015**, *5* (11), 6440−6452.
(55) Matsubara, Y. Standard Electrode Potentials for the Reduction of CO_2 to CO in Acetonitrile-Water Mixtures Determined Using a Generalized Method for Proton-Coupled Electron-Transfer Reactions. *ACS Energy Lett.* **2017**, *2* (8), 1886−1891.
(56) Bard, A. J.; Parsons, R.; Jordan, J. *Standard Potentials in Aqueous Solution*; M. Dekker, New York, 1985.
(57) Pavlishchuk, V. V.; Addison, A. W. Conversion Constants for Redox Potentials Measured versus Different Reference Electrodes in Acetonitrile Solutions at 25°C. *Inorg. Chim. Acta* **2000**, *298* (1), 97−102.
(58) Hooe, S. L.; Dressel, J. M.; Dickie, D. A.; Machan, C. W. Highly Efficient Electrocatalytic Reduction of CO_2 to CO by a Molecular Chromium Complex. *ACS Catal.* **2020**, *10* (2), 1146−1151.
(59) Ngo, K. T.; McKinnon, M.; Mahanti, B.; Narayanan, R.; Grills, D. C.; Ertem, M. Z.; Rochford, J. Turning on the Protonation-First Pathway for Electrocatalytic CO_2 Reduction by Manganese Bipyridyl Tricarbonyl Complexes. *J. Am. Chem. Soc.* **2017**, *139* (7), 2604−2618.
(60) Dey, S.; Ahmed, M. E.; Dey, A. Activation of Co(I) State in a Cobalt-Dithiolato Catalyst for Selective and Efficient CO_2 Reduction to CO. *Inorg. Chem.* **2018**, *57* (10), 5939−5947.
(61) Ahmed, M. E.; Rana, A.; Saha, R.; Dey, S.; Dey, A. Homogeneous Electrochemical Reduction of CO_2 to CO by a Cobalt Pyridine Thiolate Complex. *Inorg. Chem.* **2020**, *59* (8), 5292−5302.
(62) Lee, K. J.; McCarthy, B. D.; Dempsey, J. L. On Decomposition, Degradation, and Voltammetric Deviation: The Electrochemist's Field Guide to Identifying Precatalyst Transformation. *Chem. Soc. Rev.* **2019**, *48* (11), 2927−2945.
(63) Rountree, E. S.; McCarthy, B. D.; Eisenhart, T. T.; Dempsey, J. L. Evaluation of Homogeneous Electrocatalysts by Cyclic Voltammetry. *Inorg. Chem.* **2014**, *53* (19), 9983−10002.
(64) Costentin, C.; Drouet, S.; Robert, M.; Savéant, J.-M. Turnover Numbers, Turnover Frequencies, and Overpotential in Molecular Catalysis of Electrochemical Reactions. Cyclic Voltammetry and Preparative-Scale Electrolysis. *J. Am. Chem. Soc.* **2012**, *134* (27), 11235−11242.
(65) Costentin, C.; Drouet, S.; Robert, M.; Savéant, J.-M. Correction to Turnover Numbers, Turnover Frequencies, and Overpotential in Molecular Catalysis of Electrochemical Reactions. Cyclic Voltammetry and Preparative-Scale Electrolysis. *J. Am. Chem. Soc.* **2012**, *134* (48), 19949−19950.
(66) Galan, B. R.; Schöffel, J.; Linehan, J. C.; Seu, C.; Appel, A. M.; Roberts, J. A. S.; Helm, M. L.; Kilgore, U. J.; Yang, J. Y.; DuBois, D. L.; Kubiak, C. P. Electrocatalytic Oxidation of Formate by $[Ni(P^R_2N^{R'}_2)_2(CH_3CN)]^{2+}$ Complexes. *J. Am. Chem. Soc.* **2011**, *133* (32), 12767−12779.
(67) Sung, S.; Kumar, D.; Gil-Sepulcre, M.; Nippe, M. Electrocatalytic CO_2 Reduction by Imidazolium-Functionalized Molecular Catalysts. *J. Am. Chem. Soc.* **2017**, *139* (40), 13993−13996.
(68) Haviv, E.; Azaiza-Dabbah, D.; Carmieli, R.; Avram, L.; Martin, J. M. L.; Neumann, R. A Thiourea Tether in the Second Coordination Sphere as a Binding Site for CO_2 and a Proton Donor Promotes the Electrochemical Reduction of CO_2 to CO Catalyzed by a Rhenium Bipyridine-Type Complex. *J. Am. Chem. Soc.* **2018**, *140* (39), 12451−12456.
(69) Chapovetsky, A.; Welborn, M.; Luna, J. M.; Haiges, R.; Miller, T. F.; Marinescu, S. C. Pendant Hydrogen-Bond Donors in Cobalt Catalysts Independently Enhance CO_2 Reduction. *ACS Cent. Sci.* **2018**, *4* (3), 397−404.
(70) Rudd, D. J.; Goldsmith, C. R.; Cole, A. P.; Stack, T. D. P.; Hodgson, K. O.; Hedman, B. X-Ray Absorption Spectroscopic Investigation of the Spin-Transition Character in a Series of Single-Site Perturbed Iron(II) Complexes. *Inorg. Chem.* **2005**, *44* (5), 1221−1229.
(71) Gütlich, P.; Eckhard, B.; Trautwein, A. X. *Mössbauer Spectroscopy and Transition Metal Chemistry Fundamentals and Applications*; Springer: Berlin, 2011.
(72) Scarborough, C. C.; Lancaster, K. M.; DeBeer, S.; Weyhermüller, T.; Sproules, S.; Wieghardt, K. Experimental Fingerprints for Redox-Active Terpyridine in $[Cr(tpy)_2](PF_6)_n$ (n = 3−0), and the Remarkable Electronic Structure of $[Cr(tpy)_2]^{1-}$. *Inorg. Chem.* **2012**, *51* (6), 3718−3732.
(73) England, J.; Scarborough, C. C.; Weyhermüller, T.; Sproules, S.; Wieghardt, K. Electronic Structures of the Electron Transfer Series $[M(bpy)_3]^n$, $[M(tpy)^2]^n$, and $[Fe(^tbpy)_3]^n$ (M = Fe, Ru; n = 3+, 2+, 1+, 0, 1-): A Mössbauer Spectroscopic and DFT Study. *Eur. J. Inorg. Chem.* **2012**, 4605−4621.
(74) Garino, C.; Gobetto, R.; Nervi, C.; Salassa, L.; Rosenberg, E.; Ross, J. B. A.; Chu, X.; Hardcastle, K. I.; Sabatini, C. Spectroscopic and Computational Studies of a Ru(II) Terpyridine Complex: The Importance of Weak Intermolecular Forces to Photophysical Properties. *Inorg. Chem.* **2007**, *46* (21), 8752−8762.
(75) Römelt, C.; Song, J.; Tarrago, M.; Rees, J. A.; van Gastel, M.; Weyhermüller, T.; DeBeer, S.; Bill, E.; Neese, F.; Ye, S. Electronic Structure of a Formal Iron(0) Porphyrin Complex Relevant to CO_2 Reduction. *Inorg. Chem.* **2017**, *56* (8), 4745−4750.
(76) Kang, P.; Meyer, T. J.; Brookhart, M. Selective Electrocatalytic Reduction of Carbon Dioxide to Formate by a Water-Soluble Iridium Pincer Catalyst. *Chem. Sci.* **2013**, *4* (9), 3497−3502.
(77) Costentin, C.; Robert, M.; Savéant, J.-M.; Tatin, A. Efficient and Selective Molecular Catalyst for the CO_2-to-CO Electrochemical Conversion in Water. *Proc. Natl. Acad. Sci. U. S. A.* **2015**, *112* (22), 6882−6886.
(78) Taheri, A.; Thompson, E. J.; Fettinger, J. C.; Berben, L. A. An Iron Electrocatalyst for Selective Reduction of CO_2 to Formate in Water: Including Thermochemical Insights. *ACS Catal.* **2015**, *5* (12), 7140−7151.
(79) Nakada, A.; Ishitani, O. Selective Electrocatalysis of a Water-Soluble Rhenium(I) Complex for CO_2 Reduction Using Water As an Electron Donor. *ACS Catal.* **2018**, *8* (1), 354−363.
(80) Gu, J.; Hsu, C.-S.; Bai, L.; Chen, H. M.; Hu, X. Atomically Dispersed Fe^{3+} Sites Catalyze Efficient CO_2 Electroreduction to CO. *Science* **2019**, *364* (6445), 1091−1094.

https://dx.doi.org/10.1021/jacs.0c10664
J. Am. Chem. Soc. 2020, 142, 20489−20501